

# Journal of the Atmospheric Sciences

## Diagnosis of Middle Atmosphere Climate Sensitivity by the Climate Feedback Response Analysis Method

--Manuscript Draft--

<b>Manuscript Number:</b>	
<b>Full Title:</b>	Diagnosis of Middle Atmosphere Climate Sensitivity by the Climate Feedback Response Analysis Method
<b>Article Type:</b>	Article
<b>Corresponding Author:</b>	Xun Zhu Johns Hopkins University Laurel, UNITED STATES
<b>Corresponding Author's Institution:</b>	Johns Hopkins University
<b>First Author:</b>	Xun Zhu
<b>Order of Authors:</b>	Xun Zhu Jeng-Hwa Yee Ming Cai William H. Swartz Lawrence Coy Valentina Aquila Elsayed R. Talaat
<b>Abstract:</b>	<p>We present a new method to diagnose the middle atmosphere climate sensitivity by extending the Climate Feedback-Response Analysis Method (CFRAM) for the coupled atmosphere-surface system to the middle atmosphere. The Middle atmosphere CFRAM (MCFRAM) is built on the atmospheric energy equation per unit mass with radiative heating and cooling rates as its major thermal energy sources. MCFRAM preserves the CFRAM unique feature of an additive property for which the sum of all partial temperature changes due to variations in external forcing and feedback processes equals the observed temperature change. In addition, MCFRAM establishes a physical relationship of radiative damping between the energy perturbations associated with various feedback processes and temperature perturbations associated with thermal responses. MCFRAM is applied to both measurements and model output fields to diagnose the middle atmosphere climate sensitivity. It is found that the largest component of the middle atmosphere temperature response to the 11-year solar cycle (solar maximum vs. solar minimum) is directly from the partial temperature change due to the variation of the input solar flux. Increasing CO<sub>2</sub> always cools the middle atmosphere with time whereas partial temperature change due to O<sub>3</sub> variation could be either positive or negative. The partial temperature changes due to different feedbacks show distinctly different spatial patterns. The thermally driven globally averaged partial temperature change due to all radiative processes is approximately equal to the observed temperature change, ranging from -0.5 K near 25 km to -1.0 K near 70 km from the near solar maximum to the solar minimum.</p>
<b>Suggested Reviewers:</b>	<p>Roland Garcia rgarcia@ucar.edu</p> <p>K. K. Tung tung@amath.washington.edu</p> <p>Paul Newman Paul.A.Newman@nasa.gov</p> <p>Steven Pawson steven.pawson-1@nasa.gov</p> <p>Brian Soden</p>



1  
2  
3 **Diagnosis of Middle Atmosphere Climate Sensitivity by the**  
4 **Climate Feedback Response Analysis Method**

5  
6 Xun Zhu<sup>1</sup>, Jeng-Hwa Yee<sup>1</sup>, Ming Cai<sup>2</sup>, William H. Swartz<sup>1</sup>, Lawrence Coy<sup>3</sup>,  
7 Valentina Aquila<sup>4</sup>, and Elsayed R Talaat<sup>5</sup>

8  
9 <sup>1</sup> The Johns Hopkins University Applied Physics Laboratory, 11100 Johns Hopkins Road, Laurel, MD 20723

10 <sup>2</sup> Department of Earth, Ocean and Atmospheric Science, The Florida State University, Tallahassee, FL 21218

11 <sup>3</sup> Science Systems and Applications, Inc, 10210 Greenbelt Road, Lanham, MD 20706

12 <sup>4</sup> GESTAR/Johns Hopkins University, 3400 N Charles Street, Baltimore, MD 21218

13 <sup>5</sup> Heliophysics Division, NASA Headquarters, Washington, D.C. 20546

14  
15  
16 Submitted to *Journal of the Atmospheric Sciences*

17 August 26, 2014

18  
19  
20  
21  
22 *Corresponding author address:*

23  
24 Dr. Xun Zhu  
25 The Johns Hopkins University  
26 Applied Physics Laboratory  
27 11100 Johns Hopkins Road  
28 Laurel, MD 20723-6099  
29 Phone: 443-778-8764  
30 Fax: 443-778-6670  
31 E-mail: xun.zhu@jhuapl.edu  
32

33

34 **Abstract**

35         We present a new method to diagnose the middle atmosphere climate sensitivity by  
36 extending the Climate Feedback-Response Analysis Method (CFRAM) for the coupled  
37 atmosphere-surface system to the middle atmosphere. The Middle atmosphere CFRAM  
38 (MCFRAM) is built on the atmospheric energy equation per unit mass with radiative heating and  
39 cooling rates as its major thermal energy sources. MCFRAM preserves the CFRAM unique  
40 feature of an additive property for which the sum of all partial temperature changes due to  
41 variations in external forcing and feedback processes equals the observed temperature change. In  
42 addition, MCFRAM establishes a physical relationship of radiative damping between the energy  
43 perturbations associated with various feedback processes and temperature perturbations  
44 associated with thermal responses. MCFRAM is applied to both measurements and model output  
45 fields to diagnose the middle atmosphere climate sensitivity. It is found that the largest  
46 component of the middle atmosphere temperature response to the 11-year solar cycle (solar  
47 maximum vs. solar minimum) is directly from the partial temperature change due to the variation  
48 of the input solar flux. Increasing CO<sub>2</sub> always cools the middle atmosphere with time whereas  
49 partial temperature change due to O<sub>3</sub> variation could be either positive or negative. The partial  
50 temperature changes due to different feedbacks show distinctly different spatial patterns. The  
51 thermally driven globally averaged partial temperature change due to all radiative processes is  
52 approximately equal to the observed temperature change, ranging from -0.5 K near 25 km to  
53 -1.0 K near 70 km from the near solar maximum to the solar minimum.

54

55 **1. Introduction**

56 The warming of Earth's surface and lower atmosphere is associated with enhanced  
57 middle atmosphere cooling and a strengthening of the Brewer-Dobson circulation through  
58 radiative, dynamical, and photochemical coupling. Because both the air density and the optical  
59 depths of major radiatively active species decrease with altitude, the physical state of the middle  
60 atmosphere as represented by various parameters such as temperature and winds is quite  
61 sensitive to climate forcing and is thus a good indicator of surface global warming. Hence, a  
62 more accurate quantification of the middle atmosphere responses to solar variability and  
63 anthropogenic changes in trace species is necessary to improve predictions of climate change.

64 The Climate Feedback–Response Analysis Method (CFRAM) has been developed for  
65 separating and estimating various climate feedbacks in the coupled troposphere-ocean system  
66 (Lu and Cai 2009; Cai and Lu 2009; hereafter LC09 and CL09). CFRAM is formulated based on  
67 the atmosphere-surface energy equation, and it explicitly decomposes the directly *measurable*  
68 total temperature change into partial temperature changes due to individual external forcing and  
69 feedback processes (LC09, CL09). The unique feature of CFRAM is that this decomposition into  
70 partial temperature changes is locally *additive*, so that the total temperature change is the sum of  
71 all the partial temperature changes at every spatial point. From the modeling perspective, the so-  
72 called external forcing and its variation of a system are akin to independent variables or  
73 parameters that would be prescribed as input values in a model. On the other hand, the feedback  
74 or internal processes of a system are similar to dependent variables or parameters that often  
75 constitute a set of model output values.

76 In this paper, CFRAM is extended to the middle atmosphere based on three physical  
77 features of this region: (i) radiative energy exchange plays a major role in the energy budget; (ii)  
78 the air density varies with altitude by several orders of magnitude and the energy deposition per  
79 unit mass is often scaled by a factor that slowly varies with altitude or log-pressure; and (iii) the  
80 energy flux associated with the level of the Earth's surface and the layered middle atmosphere

81 are not directly coupled. As a result, the Middle atmosphere Climate Feedback–Response  
 82 Analysis Method (MCFRAM) is formulated by the energy equation in a form of heating and  
 83 cooling rates per unit mass in a commonly used unit of  $\text{K day}^{-1}$ . Its mathematical form is similar  
 84 to a well-documented radiative transfer technique for analyzing radiative damping or relaxation  
 85 of the atmospheric temperature disturbances (*e.g.*, Goody and Yung 1989, Zhu and Strobel  
 86 1991). The newly developed MCFRAM is here applied to the middle atmosphere to derive  
 87 various partial temperature changes based on both satellite measurements and output of a three-  
 88 dimensional (3D) chemistry-climate model (CCM).

89 In Section 2, we briefly review and extend CFRAM to the middle atmosphere. Then, we  
 90 perform the fundamental eigenmode analysis to the generalized damping matrix derived from the  
 91 MCFRAM. The middle atmosphere temperature and ozone fields needed in the analysis are  
 92 derived from the Sounding of the Atmosphere using Broadband Emission Radiometer (SABER)  
 93 onboard the Thermosphere, Ionosphere Mesosphere, Energetics and Dynamics (TIMED)  
 94 satellite. Section 3 shows the MCFRAM results derived from the SABER measurements whereas  
 95 section 4 performs a set of similar MCFRAM analyses on the output fields of the Goddard Earth  
 96 Observing System chemistry-climate model (GEOSCCM; Pawson *et al.*, 2008, and references  
 97 therein). Section 5 summarizes the paper.

## 98 **2. Review and extension of the Coupled Feedback Response Analysis Method**

### 99 **2.1 Formulation of the middle atmosphere CFRAM**

100 CFRAM was originally formulated in a form of a vertical energy flux difference for a  
 101 single-column energy equation in a form of the time mean energy balance equation (LC09;  
 102 CL09):

$$103 \mathbf{R}^*(\mathbf{T}, r, s, \dots, \alpha, \beta, \dots) = \mathbf{S}^*(\mathbf{T}, r, s, \dots, \alpha, \beta, \dots) + \mathbf{Q}^*(\mathbf{T}, r, s, \dots, \alpha, \beta, \dots), \quad (1)$$

104 where  $\mathbf{R}^*$  and  $\mathbf{S}^*$  are the infrared and solar flux differences corresponding to total radiative  
 105 cooling and heating of a layered atmosphere, respectively.  $\mathbf{Q}^*$  is the non-radiative energy flux  
 106

107 convergence in the atmospheric layers.  $\mathbf{T}$  is temperature profile,  $(r, s, \dots)$  are the mixing ratios of  
 108 radiatively active species such as  $\text{CO}_2$ ,  $\text{O}_3$ ,  $\text{H}_2\text{O}$  and clouds, and  $(\alpha, \beta, \dots)$  are the parameters  
 109 such as the solar irradiance, surface albedo and solar declination angle that will affect the  
 110 atmospheric energy. The terms in the energy Eq. (1) for CFRAM have the units of energy flux  
 111  $\text{W m}^{-2}$ , which corresponds to the heating or the cooling rate per unit volume for a given layer of  
 112 atmosphere. There are several advantages of adopting the flux form with units  $\text{W m}^{-2}$  in the  
 113 classic CFRAM: (i) the energy flux of the atmosphere can be naturally coupled with the surface  
 114 energy flux; (ii) the top of the atmosphere (TOA) version of CFRAM can be directly compared  
 115 to a TOA-based climate feedback analysis such as the partial radiative perturbation (PRP)  
 116 method; (iii) the layer thickness of the tropospheric CCMs is usually slowly varying in mass so  
 117 the heating or cooling rate perturbations per unit space of different layers also slowly vary with  
 118 altitude.

119 The air density decreases with altitude exponentially in the middle atmosphere, ranging  
 120 from the tropopause ( $\sim 10$  km) to the turbopause ( $\sim 110$  km), spanning several orders of  
 121 magnitude in density variation. The energy deposition or the atmospheric heating rate in  
 122 measurements and models is often scaled in a unit mass with a setting in vertical grid that slowly  
 123 varies with altitude or log-pressure. As a result, we begin by developing our MCFRAM from an  
 124 energy equation per unit mass, *i.e.*, by dividing Eq. (1) by  $c_p \rho \Delta z$  with  $c_p$ ,  $\rho$  and  $\Delta z$  being the  
 125 specific heat at constant pressure, air density and layer thickness, respectively,

$$126 \quad \mathbf{R}(\mathbf{T}, r, s, \dots, \alpha, \beta, \dots) = \mathbf{S}(\mathbf{T}, r, s, \dots, \alpha, \beta, \dots) + \mathbf{Q}(\mathbf{T}, r, s, \dots, \alpha, \beta, \dots) + \mathbf{Q}_{mol}(\mathbf{T}), \quad (2)$$

128 where  $\mathbf{R}$  and  $\mathbf{S}$  are the radiative cooling and heating rates, respectively.  $\mathbf{Q}$  is the non-radiative  
 129 heating rate excluding the molecular thermal conductivity  $\mathbf{Q}_{mol}(\mathbf{T})$  that is only a function of  
 130 temperature profile  $\mathbf{T}$  (Banks and Kockarts 1973). The units of all terms in Eq. (2) are  $\text{K day}^{-1}$ .  
 131 We now consider two statistical equilibrium states 1 and 2 with two different sets of  
 132 corresponding atmospheric parameters all satisfying the energy balance equation (2). In practice,

133 these two states can be two ensemble, time or spatially averaged mean states. The difference of  
 134 the energy equations between these two states is

$$135 \Delta(\mathbf{R} - \mathbf{Q}_{mol}) = \Delta\mathbf{S} + \Delta\mathbf{Q}. \quad (3)$$

137 We now introduce the linear approximation to the responses of  $\mathbf{R}$  and  $\mathbf{Q}_{mol}$  to the temperature  
 138 variation and separate this term from the variations due to other parameters:

$$139 \Delta(\mathbf{R} - \mathbf{Q}_{mol}) \approx \frac{\partial(\mathbf{R} - \mathbf{Q}_{mol})}{\partial\mathbf{T}} \Delta\mathbf{T} + [\mathbf{R}(\bar{\mathbf{T}}, r_2, s_2, \dots, \alpha_2, \beta_2, \dots) - \mathbf{R}(\bar{\mathbf{T}}, r_1, s_1, \dots, \alpha_1, \beta_1, \dots)], \quad (4)$$

141 where  $\bar{\mathbf{T}}$  is the “mean temperature profile” between profiles  $\mathbf{T}_1$  and  $\mathbf{T}_2$ . Substituting Eq. (4) into  
 142 Eq. (3), we obtain

$$143 \Delta\mathbf{T} = \mathbf{A}^{-1} \{ \Delta\mathbf{S} - \Delta'\mathbf{R} + \Delta\mathbf{Q} \}, \quad (5)$$

145 where  $\mathbf{A} \equiv \partial(\mathbf{R} - \mathbf{Q}_{mol}) / \partial\mathbf{T} \approx \Delta(\mathbf{R} - \mathbf{Q}_{mol}) / \Delta\mathbf{T}$  is the generalized damping matrix in units of  
 146 day<sup>-1</sup> and  $\Delta'\mathbf{R}$  defined by the last two terms in Eq. (4) is the change in total cooling rate due to  
 147 all parameters except the temperature profile.

148 In CFRAM, where the surface and the atmosphere are strongly coupled radiatively and  
 149 dynamically, the discretization of the energy equation (1) and the derivation of the “Planck  
 150 feedback matrix”  $\partial\mathbf{R}^* \partial\mathbf{T}$  based on the temperature profile need to include the temperatures of  
 151 both the surface level and layers of the atmosphere (LC09). The surface temperature and  
 152 atmospheric temperature are treated as equally important in the setting of the problem. As a  
 153 result, Eq. (1) needs to be in the form of energy flux divergence in units of energy flux  $\text{W m}^{-2}$ .  
 154 The temperature profile in the middle atmosphere is not directly coupled to the Earth surface. It  
 155 can therefore be discretized solely based on a layered atmosphere in an energy equation of unit  
 156 mass (Eq. 2). The effect of the energy flux emergent from the lower boundary on the middle  
 157 atmosphere is primarily the radiative flux that is independent of the temperature in the middle  
 158 atmosphere. For example, the effect of the solar radiative flux can often be parameterized by an  
 159 effective albedo of the surface and lower atmosphere ( $\omega_0$ ), which enhances the heating rate due



160 to absorption of the Chappuis bands (410-750 nm) by ozone in the stratosphere caused by  
 161 surface reflection and multiple scattering of clouds, aerosols and air (*e.g.*, Meier *et al.* 1982;  
 162 Nicolet *et al.* 1982). The calculation of the generalized damping matrix  $\mathbf{A}$  for a basic state of  
 163 temperature and species distributions can be implemented by a radiation algorithm and molecular  
 164 diffusive formulation. In this paper, the Johns Hopkins University Applied Physics Laboratory  
 165 (JHU/APL) middle atmosphere radiation algorithm (Zhu 1994, 2004) is adopted for radiative  
 166 cooling calculations, and a temperature-dependent thermal conductivity of  $\lambda = 5.6 \times 10^{-4} T^{0.69}$   
 167 [ $\text{kg} \cdot \text{m} \cdot \text{s}^{-3} \cdot \text{K}^{-1}$ ] (Banks and Kockarts 1973) is used for calculating the diffusive heat flux of  
 168  $\lambda \partial T / \partial z$ . Each column (vertical axis) of  $\mathbf{A}$  represents the vertical profile of cooling rate and  
 169 diffusive heating rate difference ( $\text{K day}^{-1}$ ) due to a unit change in temperature at altitude  $z$   
 170 (horizontal axis).

171 In the middle atmosphere, the effect of line overlap is negligible for the infrared radiative  
 172 cooling rate calculations. As a result, the total infrared cooling rate can be evaluated as the sum  
 173 of the cooling rates due to  $\text{CO}_2$ ,  $\text{O}_3$  and  $\text{H}_2\text{O}$  (Zhu 1994). Therefore, the term  $\Delta' \mathbf{R}$  in Eq. (4) or  
 174 (5) becomes,

$$175 \Delta' \mathbf{R} = \Delta \mathbf{R}^{\text{CO}_2} + \Delta \mathbf{R}^{\text{O}_3} + \Delta \mathbf{R}^{\text{H}_2\text{O}}. \quad (6)$$

177 Note that for the middle atmosphere, Eq. (6) is nearly exactly satisfied. In other words, the linear  
 178 separation of the partial infrared radiative cooling rate due to individual gases in the middle  
 179 atmosphere is satisfied automatically, which is not the case for the troposphere. Therefore, the  
 180 only linear approximation introduced to the infrared radiative cooling rate is the separation of the  
 181 temperature variation, as indicated in Eq. (4). In this sense, fewer approximations for the middle  
 182 atmosphere feedback analysis have been used than those for the troposphere and surface  
 183 temperatures, *e.g.*, the CFRAM (LC09) and PRP method (Soden *et al.* 2008).

184 For radiative heating by solar flux, we still need to invoke a linear approximation to  
 185 decompose the energy perturbation into individual components by different factors, namely,

186

187

$$\Delta \mathbf{S} \approx \frac{\partial \mathbf{S}}{\partial [\text{O}_3]} \Delta [\text{O}_3] + \frac{\partial \mathbf{S}}{\partial [\text{O}_2]} \Delta [\text{O}_2] + \frac{\partial \mathbf{S}}{\partial F_{107}} \Delta F_{107} + \frac{\partial \mathbf{S}}{\partial \omega_0} \Delta \omega_0, \quad (7a)$$

188 or

189

190

$$\Delta \mathbf{S} \approx \Delta \mathbf{S}^{\text{O}_3} + \Delta \mathbf{S}^{\text{O}_2} + \Delta \mathbf{S}^{\text{F}_{107}} + \Delta \mathbf{S}^{\omega_0}, \quad (7b)$$

191

192

193

194

195

196

197

198

199

200

where  $[\text{O}_3]$  and  $[\text{O}_2]$  are the ozone and oxygen densities, respectively.  $F_{107}$  is the 10.7-cm solar radio flux (in units of  $10^{-22} \text{ W m}^{-2} \text{ Hz}^{-1}$ ), which is a parameter representing the solar flux variations, and  $\omega_0$  is the effective albedo of surface and the lower atmosphere. The effect of  $[\text{O}_2]$  variation on the energy perturbation ( $\Delta \mathbf{S}^{\text{O}_2}$ ) is only important in the lower thermosphere. In the middle atmosphere, the vertical velocity associated with the meridional circulation or the residual circulation plays an important role in coupling the radiation with dynamics and photochemistry. Here, invoking a linear approximation, we may explicitly extract this special term of “dynamical response” from the total non-radiative energy source (Holton 2004):

$$\Delta \mathbf{Q} = \Theta \Delta \mathbf{w}^* + (\Delta \Theta) \mathbf{w}^* + \Delta \mathbf{Q}^{\text{eddy}}, \quad (8)$$

201

202

203

204

205

206

207

208

209

210

211

212

where the diagonal matrix  $\Theta$  is the static stability parameter and column vector  $\Delta \mathbf{w}^*$  is the variation in resolved vertical velocity that yields the change in adiabatic cooling. The last term in Eq. (8) represents the contributions due to unresolved small-scale eddies and the energy transport by horizontal wind among neighboring vertical columns. Note that although the non-radiative energy source ( $\Delta \mathbf{Q}$ ) can be evaluated from the dynamical modules during runtime of model integrations as reported in Lu and Cai (2010) and Song *et al.* (2014), it cannot be obtained directly from observations. It can also be evaluated as an energy residual term to balance the net radiative cooling rate and molecular mixing according to Eq. (3):  $\Delta \mathbf{Q} = \Delta(\mathbf{R} - \mathbf{Q}_{\text{mol}} - \mathbf{S})$ . Such an approach of using better-defined thermal forcing to diagnose mechanical forcing was also proposed in Zhu *et al.* (2001) to diagnose the dynamical fields in the middle atmosphere. As reported in Lu and Cai (2010) and Song *et al.* (2014),  $\Delta \mathbf{Q}$  inferred explicitly from dynamical fields is almost identical to that inferred as an energy residual term. Given  $\Delta \mathbf{Q}$ , we then use Eq.

213 (8) to obtain  $\Delta''\mathbf{Q}^{eddy}$  from the difference between  $\Delta\mathbf{Q}$  and the other two terms which can be  
 214 calculated from the available  $\mathbf{T}$  and  $\mathbf{w}^*$  profiles.

215 Substituting Eqs. (6)-(8) into Eq. (5), we obtain

$$216 \quad \Delta\mathbf{T} = \mathbf{Z} \cdot \{ -\Delta\mathbf{R}^{CO_2} + (\Delta\mathbf{S}^{O_3} - \Delta\mathbf{R}^{O_3}) + \Delta\mathbf{S}^{F107} - \Delta\mathbf{R}^{H_2O} \\ 217 \quad + \Delta\mathbf{S}^{\omega_0} + \Theta\Delta\mathbf{w}^* + (\Delta\Theta)\mathbf{w}^* + \Delta''\mathbf{Q}^{eddy} \}, \quad (9)$$

218 where  $\mathbf{Z} = \mathbf{A}^{-1}$  is the generalized relaxation matrix. Note that the change of  $[O_3]$  in the middle  
 219 atmosphere contributes to both radiative heating and cooling rate variations. This is similar to  
 220  $H_2O$  and clouds in the troposphere that can both radiatively heat and cool the atmosphere.

221 As indicated in LC09, Eq. (9) represents the property of additive thermal responses, *i.e.*,  
 222 the sum of the partial temperature changes ( $\Delta\mathbf{T}^{(n)}$ ) of the MCFRAM due to individual variations  
 223 of various external forcing such as  $\Delta[CO_2]$  or  $\Delta F_{107}$  and feedback processes such as  $\Delta[O_3]$  is  
 224 the total temperature change ( $\Delta\mathbf{T}^{total}$ ):

$$225 \quad \Delta\mathbf{T}^{total} = \sum_n \Delta\mathbf{T}^{(n)}, \quad (10)$$

227 where

$$228 \quad \Delta\mathbf{T}^{(n)} = \mathbf{Z} \cdot \Delta\mathbf{F}^{(n)}. \quad (11)$$

230 *Here, we define the total temperature change  $\Delta\mathbf{T}^{total}$  to be an observed quantity representing the*  
 231 *actual difference in the measured temperatures between the two equilibrium states.* The energy  
 232 perturbations  $\Delta\mathbf{F}^{(n)}$  in Eq. (11) denote various terms in the brackets on the right-hand side of Eq.  
 233 (9). Physically,  $\Delta\mathbf{T}^{(n)}$  correspond to the partial temperature changes associated with linear  
 234 atmospheric thermal responses to the energy perturbations  $\Delta\mathbf{F}^{(n)}$  caused by individual parameter  
 235 variations. Those parameter variations can either be derived from observations or from model  
 236 output. The physical meanings of these partial temperature changes ( $\Delta\mathbf{T}^{(n)}$ ) in MCFRAM are  
 237 shown in Table 1. The sum of the first six components forms the partial temperature change due  
 238 to radiative processes  $\Delta\mathbf{T}^{rad} = \Delta\mathbf{T}^{(1-6)}$ . The non-radiative partial temperature change  $\Delta\mathbf{T}^{non-rad}$   
 239 includes changes due to both the grid resolved and unresolved atmospheric motions. It should be

240 noted that  $\Delta\mathbf{T}^{rad}$  has been derived from the changes in net radiative heating rate *excluding* the  
 241 cooling rate change due to the temperature variation itself, *i.e.*, the terms  $(\Delta\mathbf{S} - \Delta'\mathbf{R})$  in Eq. (5).  
 242 One important reason that the temperature variation is singled out in Eq. (4) is that the  
 243 generalized damping matrix  $\mathbf{A}$  introduced in Eq. (5) is well-behaved and always invertible.

244 The additive relation (10) for the temperature changes is an alternative expression of the  
 245 energy Eq. (3) that too is additive. A linear transformation that singles out the total temperature  
 246 change from energy difference on the left-hand side of Eq. (3) also leads to the partial  
 247 temperature differences as shown in Eq. (11) and allows us to derive this alternative relationship.  
 248 The principal advantage of the additive relation (10) for temperature over the additive relation  
 249 (3) for energy is that  $\Delta\mathbf{T}^{total}$  on the left-hand side of Eq. (10) is a directly observed and  
 250 commonly used quantity, which can serve as a natural and standard scale for comparison.

251 In addition to temperature  $\mathbf{T}$  and its changes  $\Delta\mathbf{T}^{(n)}$ , we may also choose a different  
 252 variable to express the energy budget and its changes. For example, given a vertical profile of  
 253 “thermal response” as expressed by the temperature changes  $\Delta\mathbf{T}^{total}$  and  $\Delta\mathbf{T}^{(n)}$ , we may calculate  
 254 the corresponding *local* “dynamical response” of changes in meridional circulation by the  
 255 following linear transformation

$$256 \quad \Delta\mathbf{w}^{total} = (\mathbf{\Theta}^{-1}\mathbf{A}) \cdot \Delta\mathbf{T}^{total} \quad (12)$$

257 and

$$258 \quad \Delta\mathbf{w}^{(n)} = (\mathbf{\Theta}^{-1}\mathbf{A}) \cdot \Delta\mathbf{T}^{(n)}, \quad (13)$$

261 where we have already assumed a stable stratification of the atmosphere so that the matrix  $\mathbf{\Theta}$   
 262 never becomes singular or ill-conditioned (Holton 2004). This condition generally holds well in  
 263 the middle atmosphere. Substituting Eqs. (12)-(13) into Eq. (10) yields a different form of energy  
 264 budget equation:

$$265 \quad \Delta\mathbf{w}^{total} = \sum_n \Delta\mathbf{w}^{(n)}. \quad (14)$$

267 Again, note that in MCFRAM the total temperature change  $\Delta\mathbf{T}^{total}$  is a physical quantity that is  
 268 directly measurable. On the other hand, the total resolved *local* vertical velocity defined by Eq.  
 269 (12) is only an equivalent quantity corresponding to the observed  $\Delta\mathbf{T}^{total}$ . The physically  
 270 measurable vertical velocity is  $\Delta\mathbf{w}^*$  and is related to the contribution of an equivalent partial  
 271 temperature change via  $\Delta\mathbf{w}^* = (\mathbf{\Theta}^{-1}\mathbf{A}) \cdot \Delta\mathbf{T}^{w*}$  (Table 1).

272 It is noted that the *global* “thermal response” and “dynamical response” are closely  
 273 related in a more general perspective under the statistical equilibrium condition (Fels 1987; Zhu  
 274 *et al.* 2001). The meteorological underpinning of such a relation in a meridional plane is the  
 275 thermal wind balance. Specifically, even though the meridional circulation is driven by the  
 276 meridional gradient of the diabatic heating, the vertical gradient of the diabatic heating is exactly  
 277 balanced by the meridional gradient of the mechanical forcing (Fels 1987; Zhu *et al.* 2001). As a  
 278 result, the strengthening of the meridional circulation such as the Brewer-Dobson circulation in  
 279 the lower stratosphere can be interpreted either as a response to changes in thermal forcing or as  
 280 a response to changes in wave drag. Therefore, the spatial structures of  $\Delta\mathbf{T}^{(n)}$  derived from  
 281 MCFRAM based on the energy equation also provide us with a global insight into both the  
 282 thermal and dynamical responses in the middle atmosphere. Note that MCFRAM as outlined by  
 283 Eqs. (10)-(11) together with Table 1 generally applies to independent columns of the middle  
 284 atmosphere. The spatial structure of the derived  $\Delta\mathbf{T}^{(n)}$  is only a result of the diagnostic analysis  
 285 but is not explicitly included in the analysis procedure.

## 286 **2.2 Eigenmodes of the generalized damping matrix and illustration of MCFRAM**

288 In Eq. (5) or (9), there is a common matrix factor that linearly multiplies all the radiative  
 289 and non-radiative energy perturbation terms. As a result, both the magnitude and vertical  
 290 structure of the climate feedbacks are significantly influenced by the generalized damping matrix  
 291  $\mathbf{A}$  defined in Eq. (5) or the generalized relaxation matrix  $\mathbf{Z}$  defined in Eq. (9). Table 1 explicitly  
 292 shows that the partial temperature changes are proportional to the energy perturbation vectors  
 293  $\Delta\mathbf{F}^{(n)}$  for different processes and are modified by the same generalized relaxation matrix  $\mathbf{Z}$ .

294 Specifically, for a given vertical profile of the energy perturbation the spatial structure of partial  
 295 temperature change is completely determined and can be understood by the eigenvectors ( $\xi_i$ )  
 296 and eigenvalues ( $\lambda_i$ ) of  $\mathbf{A}$  or  $\mathbf{Z} = \mathbf{A}^{-1}$ :

$$297 \quad \mathbf{A}\xi_i = \lambda_i\xi_i \quad \text{or} \quad \mathbf{Z}\xi_i = \lambda_i^{-1}\xi_i, \quad i=1,2, \dots, N, \quad (15)$$

299 where  $N$  is the total number of vertical layers. Equation (15) indicates that the eigenvalues of  $\mathbf{Z}$   
 300 are the inverse of the eigenvalues of  $\mathbf{A}$  corresponding to the same eigenvectors. Here,  $\lambda_i$  and  $\lambda_i^{-1}$   
 301 can be called generalized damping rate and relaxation time corresponding to the perturbation  
 302 eigenvector  $\xi_i$ , respectively. In the absence of molecular viscosity ( $\mathbf{Q}_{mol} = 0$ ) the generalized  
 303 damping matrix is given by  $\mathbf{A} = \partial\mathbf{R} / \partial\mathbf{T}$ . Its eigenvalue  $\lambda_i$  happens to be the radiative damping  
 304 rate of a temperature perturbation (*e.g.*, Goody and Yung 1989, Zhu and Strobel 1991). The  
 305 effect of the vertical structure of the temperature perturbation characterized by its eigenvector  $\xi_i$   
 306 on the radiative damping rate has been well documented (Zhu and Strobel 1991, Zhu 1993). The  
 307 occurrence of the radiative damping rate in MCFRAM is a natural consequence that the basic  
 308 MCFRAM equation (9) or (10) is an energy perturbation equation. When the energy perturbation  
 309 is specifically referring to the cooling rate change in association with a temperature perturbation  
 310 that has been singled out among all the other changes, it is the radiative damping rate that  
 311 establishes the connection between the two perturbations. In general, the magnitude of  $\lambda_i$  under  
 312 non-vanishing  $\mathbf{Q}_{mol}$  conditions is proportional to the magnitudes of the radiative cooling rate and  
 313 molecular viscosity. It increases with the increasing characteristic vertical wavenumber of the  
 314 energy perturbation, *i.e.*, the wavenumber of cooling rate variation or the temperature variation.

315 The infrared radiative heat exchange by  $\text{CO}_2$  and  $\text{O}_3$  makes a major contribution whereas  
 316 cool-to-space cooling by  $\text{H}_2\text{O}$  makes a minor contribution to the radiative cooling rate in the  
 317 middle atmosphere (Zhu 1994). Here, we use the  $T$  and  $[\text{O}_3]$  observed from the SABER onboard  
 318 the TIMED satellite to derive  $\mathbf{A}$  or  $\mathbf{Z}$  and to perform the eigenmode analysis to illustrate the  
 319 general characteristics of the eigenvector of  $\mathbf{A}$  or  $\mathbf{Z}$  in the middle atmosphere. The needed global  
 320 mean  $\text{H}_2\text{O}$  profile for the radiation algorithm is derived from the 3D Goddard Earth Observing

321 System chemistry-climate model (GEOSCCM; Pawson *et al.*, 2008). In Fig. 1, we show the  
 322 TIMED/SABER measured global mean  $T$  and  $[O_3]$  averaged over a  $54^\circ\text{S}$ - $54^\circ\text{N}$  latitudinal range  
 323 and a 12-year period of 2002-2013. The SABER measurements ranging from 20 km to 110 km  
 324 in the middle atmosphere are merged with the US Standard Atmosphere in the troposphere. The  
 325 vertical resolution of all the input profiles from surface to 110 km is about 0.7 km. The radiative  
 326 heating and cooling rate calculations based on the JHU/APL radiation algorithm are performed  
 327 in the entire vertical domain of 157 layers whereas the MCFRAM analysis is applied to the top  
 328 129 layers ( $N=129$ ) that corresponds to a middle atmosphere ranging from 10 km to 110 km.  
 329 The matrix  $\mathbf{A}$  or  $\mathbf{Z}$  has dimensions of  $129 \times 129$  with 129 eigenmodes. Any given vertical profiles  
 330 of the energy perturbations ( $\Delta \mathbf{F}^{(n)}$ ) can be decomposed by a complete set of the eigenvectors,  
 331 with each component decaying, *i.e.*, relaxing to 0, at a rate proportional to the inverse of their  
 332 corresponding eigenvalues. Figures 2 shows a set of 17 selected vertical eigenmodes of the  
 333 generalized damping matrix  $\mathbf{A}$  calculated from  $T$  and  $[O_3]$  shown in Fig. 1 based on the  
 334 JHU/APL radiation algorithm (Zhu 1994, 2004). The  $\text{CO}_2$  volume mixing ratio in the calculation  
 335 is set at a 2005 level of 380 ppmv. The eigenmodes describe a quantitative relationship between  
 336 the energy perturbations and the corresponding temperature perturbations. The eigenvalues ( $\lambda_i$ )  
 337 of the selected eigenvectors ( $\xi_i$ ) range from a maximum value of  $\lambda_{\max} = 18.98 \text{ day}^{-1}$  (blue line  
 338 marked with circles in Fig. 2a) to a minimum value of  $\lambda_{\min} = 0.023 \text{ day}^{-1}$  (blue dashed line in  
 339 Fig. 2d). The vertical eigenmode of the largest damping rate corresponding to the smallest  
 340 relaxation time ( $\lambda_{\max}^{-1} = 0.053 \text{ day}$ ) is a wave packet located at 107 km with a very small  
 341 vertical scale of  $\sim 4 \text{ km}$ . That particular wavy energy perturbation will be effectively smoothed  
 342 out in a very short period and produces a very small temperature perturbation. On the other hand,  
 343 the eigenmode with the smallest damping rate has a vertical structure of a near uniform heating  
 344 or cooling near the tropopause. This mode has the largest relaxation time ( $\lambda_{\min}^{-1} = 43.4 \text{ day}$ ) that  
 345 will yield the largest response in partial temperature change for a given unit of heating or cooling  
 346 rate perturbations.

347 There are two distinct features shown in Fig. 2. First, there exists a strong scale-  
 348 dependence of the eigenvectors for the generalized damping matrix  $\mathbf{A}$ . Eigenvectors  
 349 corresponding to large-scale vertical perturbations have small eigenvalues. Second, the  
 350 magnitude of the eigenvalue decreases as the location of the characteristic perturbation shifts  
 351 from the upper middle atmosphere to the lower middle atmosphere. As a result, we note that  
 352 when the value of eigenvalue decreases as we move consecutively from panel (a) to panel (d) the  
 353 vertical scale of eigenvector increases and the location of its main perturbation shifts to the lower  
 354 altitude. This is consistent with the general nature of the radiative damping of temperature  
 355 perturbation in the middle atmosphere (*e.g.*, Goody and Yung 1989; Zhu 1993). In addition, the  
 356 effect of the molecular diffusion included in  $\mathbf{A}$  has the same general characteristics of small-scale  
 357 perturbations at a higher altitude being more effectively damped or filtered. To show the general  
 358 nature of scale-dependence and its departure from a precise one for the eigenmodes in the entire  
 359 middle atmosphere we perform a Fourier transform to all 129 eigenvectors and calculate their  
 360 power spectral densities (PSDs) (Zhu and Strobel 1991; Zhu 1991). Figure 3 shows a scatter plot  
 361 between the generalized damping rate  $\lambda_i$  and the wavenumber of the maximum peak in the PSD  
 362 for all 129 eigenvectors. Also shown in the figure are the analytic expression for the  
 363 parameterized radiative damping rate proposed in Zhu (1993) and a square fit ( $\lambda_i \sim m^2$ ) to the  
 364 diffusive damping. Because of the vertical inhomogeneity of the atmosphere, the relationship is  
 365 not single-valued. For example, a wave packet with a large vertical scale located in the  
 366 mesopause could have the same damping rate as one in the stratosphere with a small vertical  
 367 scale. A better parameterization for radiative damping in practice is to introduce a scale-  
 368 dependent radiative damping rate that also varies with altitude (Fels 1982; Zhu 1993).

369 The effect of the vertical structure of the energy perturbations on the partial temperature  
 370 changes through  $\mathbf{A}$  or  $\mathbf{Z}$  can be seen from Fig. 4 where the partial temperature changes of  $\Delta\mathbf{T}^{\text{CO}_2}$ ,  
 371  $\Delta\mathbf{T}^{\text{O}_3}$  and  $\Delta\mathbf{T}^{\text{F}107}$  are calculated from Table 1 based on three energy perturbations caused by  
 372 changing three atmospheric parameters (i)  $\text{CO}_2$  volume mixing ratio is doubled from 380 ppmv



373 to 760 ppmv, (ii) O<sub>3</sub> volume mixing ratio is uniformly reduced by 50%, and (iii) solar index F<sub>10.7</sub>  
374 is increased from 60 to 260 (in units of 10<sup>-22</sup> W m<sup>-2</sup>Hz<sup>-1</sup>). The vertical structure of temperature  
375 difference (Fig. 4b) is smoother than and significantly different from that of the heating rate  
376 variations (Fig. 4a). This is mainly due to the scale-dependence of the generalized damping rate  
377 ( $\lambda_i$ ) where smaller scale energy perturbations are more effectively damped, *i.e.*, partial  
378 temperature changes are smoother than energy perturbations. Furthermore, the lower middle  
379 atmosphere is more sensitive in partial temperature changes to a smaller energy perturbation due  
380 to greater opacity than the upper middle atmosphere.

### 381 **3. Application of MCFRAM to TIMED/SABER measurements**

382 Application of MCFRAM is straightforward once the input fields of various parameter  
383 variations as indicated in Eqs. (5) and (9) together with Table 1 are available. While climate  
384 models (such as the GEOSCCM) can provide all the needed and uniformly distributed global  
385 input fields, satellite measurements often provide only part of the needed fields to derive the  
386 balanced additive relation (10). In this section, we show the MCFRAM analyzed results by using  
387 SABER measured  $T$  and O<sub>3</sub> fields (Russell *et al.* 1999). We use the V1.07 SABER data available  
388 to the public from the TIMED mission data center (<http://www.timed.jhuapl.edu>) which yields  
389 significantly improved temperature retrievals at high latitude summer (Kutepov *et al.* 2006).

390 Figures 5a and 5b show the zonal mean  $T$  and O<sub>3</sub> fields in the middle atmosphere derived  
391 from SABER measurements in the low and mid-latitudes averaged over a 12-year period of  
392 2002-2013. Shown in Figs. 5c and 5d are the  $T$  and O<sub>3</sub> difference between two time-mean states  
393 covering the periods of 2002-2003 and 2008-2009, respectively. Though the overall temperature  
394 in the middle atmosphere exhibits a noticeable decrease from the 2002-2003 period of near solar  
395 maximum to the 2008-2009 period of solar minimum over most regions, there are some regions  
396 showing positive temperature anomalies in response to the solar energy input decrease. We note  
397 that the observed temperature difference represents the total effects contributed by various

398 processes including the solar flux changes due to solar cycle and man-made variations in CO<sub>2</sub>  
 399 concentration and other chemical species.

400 We now apply MCFRAM to the SABER observed  $T$  and O<sub>3</sub> difference between two  
 401 periods of 2002-2003 and 2008-2009. The corresponding mean CO<sub>2</sub> mixing ratios and solar flux  
 402 indices used in MCFRAM analysis for these two periods are [ $r_{\text{CO}_2} \sim 374.7$  ppmv,  $F_{10.7} \sim 167.1$ ] and  
 403 [ $r_{\text{CO}_2} \sim 386.3$  ppmv,  $F_{10.7} \sim 68.1$ ], respectively. There are 12 yaw cycles in each two-year period  
 404 with each yaw cycle covering about 60 days. The corresponding local time and latitudinal  
 405 coverage in two yaw cycles separated by six years are nearly identical. The temperature  
 406 difference shown in Fig. 5c represents the total temperature difference  $\Delta \mathbf{T}^{\text{total}}$  as defined in Eq.  
 407 (10). The MCFRAM analysis is performed separately to the corresponding yaw cycles with the  
 408 seasonal parameters such as the solar declination angle and  $F_{10.7}$  varying with different yaw  
 409 cycles. The partial temperature changes as defined in Eq. (11) or Table 1 will be the 12-yaw  
 410 cycle mean of all partial temperature changes between the two yaw cycles in the corresponding  
 411 time periods separated by 6 years. Given the observed  $T$ , O<sub>3</sub> and  $F_{10.7}$  variations and using the  
 412 JHU/APL middle atmosphere radiation algorithm, the first three components of the partial  
 413 temperature changes shown in Table 1, *i.e.*,  $\Delta \mathbf{T}^{\text{CO}_2}$ ,  $\Delta \mathbf{T}^{\text{O}_3}$  and  $\Delta \mathbf{T}^{\text{F}_{10.7}}$ , can be explicitly  
 414 evaluated. Since H<sub>2</sub>O and other radiatively active species only make minor contributions to the  
 415 radiative heating and cooling rate in the middle atmosphere, we expect the sum of the above  
 416 three terms is approximately the partial temperature change due to radiative transfer  $\Delta \mathbf{T}^{\text{rad}}$  as  
 417 described in Table 1. As mentioned before, we use the energy residual of Eq. (3) to estimate  $\Delta \mathbf{Q}$   
 418 to calculate  $\Delta \mathbf{T}^{\text{non-rad}}$ . In Fig. 6, we show the latitude-altitude distributions of  $\Delta \mathbf{T}^{\text{CO}_2}$ ,  $\Delta \mathbf{T}^{\text{O}_3}$ ,  
 419  $\Delta \mathbf{T}^{\text{F}_{10.7}}$  and  $\Delta \mathbf{T}^{\text{non-rad}}$ . Also shown in the figure are  $\Delta \mathbf{w}^{\text{CO}_2}$  defined by Eq. (13) and the error in  
 420  $\Delta \mathbf{T}^{\text{non-rad}}$  due to linearization, *i.e.*, the difference between  $\Delta \mathbf{T}^{\text{non-rad}}$  based on the energy residual  
 421 (Table 1) and the one based on a temperature residual  $\Delta \mathbf{T}^{\text{total}} - (\Delta \mathbf{T}^{\text{CO}_2} + \Delta \mathbf{T}^{\text{O}_3} + \Delta \mathbf{T}^{\text{F}_{10.7}})$ .

422 We note that the middle atmosphere cooling rate by the CO<sub>2</sub> 15- $\mu\text{m}$  band is mainly  
 423 contributed from its cool-to-space component with its escape probability slowly varying with

424 altitude in the middle atmosphere (Zhu *et al.* 1992). A uniform change in CO<sub>2</sub> mixing ratio also  
 425 leads to a near uniform change in escape probability in the middle atmosphere. Hence, the  
 426 maximum response to a uniform increase in CO<sub>2</sub> mixing ratio in the middle atmosphere occurs  
 427 at the equatorial stratopause (Fig. 6a), where the peak temperature as shown in Fig. 5a produces  
 428 the largest cooling rate variation. On the other hand, the response  $\Delta T^{O_3}$  due to change in O<sub>3</sub>  
 429 concentration represents a combined effect of both the solar flux heating and O<sub>3</sub> 9.6  $\mu\text{m}$  band  
 430 infrared cooling. Since there are both positive and negative ozone variations between 2002-2003  
 431 and 2008-2009 periods (Fig. 5d), the induced partial temperature change  $\Delta T^{O_3}$  also shows a non-  
 432 uniform spatial pattern (Fig. 6b). The peak variation in temperature in the upper mesosphere is  
 433 mainly due to the change in localized absorption of solar ultraviolet (UV) flux heating whereas  
 434 the peak variations in the stratosphere are mainly due to the enhanced O<sub>3</sub> 9.6  $\mu\text{m}$  band cool-to-  
 435 space cooling rate variations in a more transparent atmosphere. Here, we note that the middle  
 436 atmosphere climate responses to the cooling rate changes induced by CO<sub>2</sub> and O<sub>3</sub> variations are  
 437 different.  $\Delta T^{CO_2}$  due to CO<sub>2</sub> variation (Fig. 6a) mostly follows the total temperature field due to  
 438 a strong dependence of outgoing infrared radiation on the Planck blackbody emission whereas  
 439  $\Delta T^{O_3}$  due to O<sub>3</sub> variation (Fig. 6b) mostly follows O<sub>3</sub> concentration due to a stronger  
 440 dependence of radiative emission on more rapidly varying escape probability (Zhu *et al.* 1991).  
 441  $\Delta T^{F107}$  shown in Fig. 6c exhibits a pattern of overall monotonic increase in magnitude with  
 442 altitude mainly due to the fact that solar UV fluxes of greater variations at shorter wavelengths  
 443 are generally absorbed at higher altitudes.

444 We note that the overall spatial pattern and magnitude of  $\Delta T^{non-rad}$  shown in Fig. 6d is  
 445 similar to  $\Delta T^{total}$  shown in Fig. 5c, indicating the importance of dynamical drive of the zonal  
 446 mean middle atmospheric thermal structure. One striking feature in Fig. 6d is that  $\Delta T^{non-rad}$  is  
 447 significantly greater and has richer spatial structure than any individual partial temperature  
 448 change due to radiation processes. In other words, most part of temperature changes in the  
 449 middle atmosphere are associated with dynamic processes and the corresponding changes in

450 thermal radiation in turn balance the non-radiative energy source. One plausible explanation is  
451 that the middle atmosphere thermal radiative forcing as a whole is largely modulated by the  
452 dynamical wave drag, which is strong due to decreasing air density with altitude and  
453 significantly inhomogeneous due to randomness of various wave generation and dissipation  
454 mechanisms. Furthermore, from a global perspective, the adiabatic heating and mechanical  
455 forcing are balanced in a zonally averaged meridional plane under the quasi-equilibrium  
456 conditions (Zhu *et al.* 2001). For example, in the lower stratosphere, because the tropopause is  
457 much higher (~17 km) in the tropics than in the extratropics (~10 km), an induced thermal  
458 cooling in the high-latitude lower stratosphere associated with  $\Delta T^{\text{CO}_2}$  coupled with a mid-  
459 tropospheric warming in the tropics would enhance a meridional gradient of diabatic heating.  
460 Such a change in thermal forcing is accompanied by an enhancement in the vertical gradient of  
461 the wave drag, which is often considered as a dynamical mechanism of driving the strengthening  
462 of the Brewer-Dobson circulation in the lower stratosphere (Butchart *et al.* 2006; Garcia and  
463 Randel 2008; Shepherd and McLandress 2011).

464 The equivalent partial change in vertical velocity due to change in  $\text{CO}_2$  as shown in Fig.  
465 6e shows a clear negative correlation to  $\Delta T^{\text{CO}_2}$  shown in Fig. 6a, indicating the fact that a  
466 decrease in atmospheric temperature can be dynamically associated with an increase in adiabatic  
467 cooling induced by a strengthening in upward motion. A magnitude of 1K in temperature  
468 decrease due to climate forcing is equivalent to an increase of about  $0.025 \text{ km day}^{-1}$  in vertical  
469 velocity in terms of atmospheric dynamical response. Comparison between Fig. 6d and 6f  
470 suggests that the linearization from an energy residual to a temperature residual leads to errors of  
471 less than 10% in partial temperature changes. This can also be considered as a measure of errors  
472 in converting the generic additive relation (3) for energy differences to the MCFRAM additive  
473 relation (10) for temperature changes.

474 Though  $\Delta T^{\text{non-rad}}$  could be very large locally, its global average in the middle atmosphere  
475 should be much smaller than its typical local values. This is mainly due to the fact that the

476 globally averaged vertical velocity at a given pressure level should nearly vanish (Olague *et al.*  
 477 1992), and the main role of propagating waves is to redistribute rather than generate the  
 478 momentum and heat (*e.g.*, Zhu *et al.* 2008, 2010). It is only the eddy diffusion generated by wave  
 479 breaking and molecular viscosity that will be able to produce a globally averaged heating or  
 480 cooling rate difference. In Fig. 7a, we plot the globally averaged partial temperature changes as  
 481 shown in Fig. 6a-d together with the sum of the three components, which gives a very good  
 482 approximation of  $\Delta T^{rad}$  in the middle atmosphere. The figure shows that  $\Delta T^{rad}$  gradually  
 483 increases from 0 near 22 km to 1K near 30 km. It remains to be  $\sim 1K$  in the region of 30-70 km.  
 484 The difference between  $\Delta T^{total}$  derived from the direct measurements by SABER and  $\Delta T^{rad}$  is  
 485  $\Delta T^{non-rad}$ . Its global mean is shown in Fig. 7b. Figure 7b confirms our conjecture that the  
 486 globally averaged  $\Delta T^{non-rad}$  is a small difference between globally averaged  $\Delta T^{total}$  and  $\Delta T^{rad}$  in  
 487 most of the middle atmosphere although locally  $\Delta T^{non-rad}$  is noticeably greater than either  $\Delta T^{total}$   
 488 or  $\Delta T^{rad}$ . Physically, Fig. 7b also means that the globally averaged climate change in the middle  
 489 atmosphere is thermally driven below  $\sim 70$  km where the vertical eddy transport due to wave  
 490 breaking is expected to be small. An increase in CO<sub>2</sub> concentration coupled with a decrease in  
 491 solar radiation reduces the net radiative heating rate, which cools the global atmosphere. It  
 492 should be pointed out that this is not an obvious scenario among several alternatives. For  
 493 example, an atmosphere can be adiabatically cooled globally at a certain altitude range by a  
 494 systematic upward motion driven by a radiative heating (*e.g.*, Zhu *et al.* 2014). Near and above  
 495 the mesopause region, globally averaged  $\Delta T^{non-rad}$  is no longer small but of the same order of  
 496 magnitude as  $\Delta T^{total}$  or  $\Delta T^{rad}$ . This is mainly because the gravity wave breaking in the upper  
 497 mesosphere induces eddy diffusion that irreversibly transports and distributes tracers including  
 498 the potential temperature associated with atmospheric energy.

499 It is worth pointing out that the results shown in Fig. 7 independently verify the SABER  
 500 measurements of  $T$  and O<sub>3</sub> and the accuracy of the JHU/APL radiation algorithm for the middle  
 501 atmosphere. One common way of verifying measurements and testing radiation algorithms is to

502 evaluate the global radiative balance (Kiehl and Solomon 1986; Olaguer *et al.* 1992). A good  
503 radiation algorithm requires the globally averaged net radiative heating rate to be much smaller  
504 than the typical values of the localized net radiative heating rate. A more stringent requirement  
505 for a good algorithm is to further have a greater sensitivity of heating or cooling rate with respect  
506 to variations in radiation parameters while still preserving the property of its globally averaged  
507 net radiative heating rate close to zero. Note that  $\Delta T^{rad}$  and  $\Delta T^{non-rad}$  are closely related to the  
508 *difference* of the net radiative heating rate and the vertical velocity between two slightly different  
509 equilibrium states, respectively. The result shown in Fig. 7a suggests that the JHU/APL radiation  
510 algorithm is sensitive to variations in CO<sub>2</sub>, O<sub>3</sub> and F<sub>10.7</sub> and yet the globally averaged  $\Delta T^{non-rad}$   
511 shown in Fig. 7b remains small, as expected for thermally driven global change, based on the  
512 premise that the SABER measured  $T$  and O<sub>3</sub> fields are accurate as well.

#### 513 **4. Application of MCFRAM to GEOSCCM output fields**

514 Similar to the SABER measurements, we apply the MCFRAM analysis to two-  
515 dimensional zonal mean fields derived from the GEOSCCM. The 3D GEOSCCM uses the  
516 GEOS-5 atmospheric general circulation model (Rienecker *et al.* 2008) in its forecast-model  
517 component, coupled with the stratospheric chemical solver developed as a part of the GSFC 3D  
518 chemical-transport model (Douglass *et al.* 1996; Pawson *et al.* 2008). With respect to Rienecker  
519 *et al.* (2008) this version of GEOSCCM also includes a treatment of stratospheric aerosol (Aquila  
520 *et al.* 2012; 2013) and a mechanism to generate the QBO using a gravity wave drag  
521 parameterization (Molod *et al.* 2012). The GEOSCCM traditionally uses a fixed input solar  
522 spectrum, representative of mean solar cycle conditions, and has in fact been used as a no-solar  
523 cycle reference model in past CCM intercomparisons (Austin *et al.*, 2008). For use in MCFRAM  
524 the GEOSCCM has been modified to include a solar cycle through the development of new  
525 atmospheric heating and photolysis code (Swartz *et al.* 2012).

526 In general, the saved fields of GEOSCCM or any other CCMs are not specifically  
527 designed for directly performing a full MCFRAM analysis. Additional processing to some of the

528 output fields is needed in order to produce a set of appropriate input fields for MCFRAM  
 529 analysis. One potentially important input parameter as shown in Eq. (7) or (9) is the effective  
 530 albedo of surface and the lower atmosphere ( $\omega_0$ ) that radiatively couples the middle atmosphere  
 531 with the troposphere and surface.  $\omega_0$  is not saved in GEOSCCM as an output field in the  
 532 simulations used. We therefore use the saved field “TOA net downward shortwave flux”  $F_{RSR}$   
 533 ( $\text{W m}^{-2}$ ) to derive  $\omega_0$ .  $F_{RSR}$  is related to  $\omega_0$  by the following relationship

$$534 \quad F_{RSR} = S_{TOA}(1 - \omega_0) = S_0\mu(1 - \omega_0), \quad (16)$$

536 where  $S_{TOA}$  is the TOA downward solar flux with  $S_0$  and  $\mu$  being the solar constant (= 1366  
 537  $\text{W m}^{-2}$ , Liou 2002) and cosine of the solar zenith angle, respectively. For a given zonal mean  
 538  $F_{RSR}$ , the diurnally averaged  $S_{TOA}$  can be calculated by (Cogley and Borucki 1976, Zhu 1994)

$$539 \quad \bar{S}_{TOA} \equiv S_0\bar{\mu} = \frac{S_0}{\pi} \int_{\max(0, A-B)}^{\max(0, A+B)} \frac{\mu d\mu}{\sqrt{B^2 - (\mu - A)^2}}, \quad (17)$$

541 where  $A = \sin\phi \sin\delta$ ,  $B = \cos\phi \cos\delta$ ,  $\phi$  is the latitude, and  $\delta$  is the solar declination angle. We  
 542 finally get the  $\omega_0$  for applying MCFRAM to a zonal mean field

$$543 \quad \omega_0 = 1 - \frac{\bar{F}_{RSR}}{\bar{S}_{TOA}}. \quad (18)$$

545 Note that when  $A+B \leq 0$  the sun does not rise and  $\bar{S}_{TOA} = 0$  and  $\omega_0$  can be any value. Under  
 546 such a circumstance, we set the variation of  $\omega_0$  between the two states 1 and 2 to be zero. When  
 547  $A-B > 0$  then the sun does not set and the lower limit of the integration in Eq. (17) is set to  
 548  $A-B$ . Since the upper boundary of the current GEOSCCM is below the mesopause, where the  
 549 effect of  $\text{O}_2$  variation is negligible in energy budget, we will neglect  $\Delta\mathbf{T}^{\text{O}_2}$  in this paper.

550 Another issue in implementing MCFRAM analysis based on model output fields is that  
 551 most CCMs such as the GEOSCCM only save separately the total solar heating and infrared  
 552 cooling rates but not the individual components contributed by different absorbers and solar flux  
 553 variations. We have already pointed out previously through Eq. (6) that the separation of cooling

554 rate components in the middle atmosphere is very simple because the effect of line overlapping  
 555 is negligible. On the other hand, Eq. (7) suggests that it requires a significant overhaul to the  
 556 online radiation code in any CCMs in order to derive and save heating rate contributions by  
 557 different components mainly because of the nonlinear effect between solar flux and absorber.  
 558 One way to get around the whole issue is to calculate all the radiative heating and cooling  
 559 perturbation terms offline and introduce two error terms to the basic MCFRAM Eqs. (10) and  
 560 (11) (Taylor *et al.* 2013; Sejas *et al.* 2014):

$$561 \quad \Delta \mathbf{T}^{total} = \sum_n \Delta \mathbf{T}^{(n)} - \Delta \mathbf{T}^{err1} - \Delta \mathbf{T}^{err2}. \quad (19)$$

563 Here, the two partial temperature changes due to radiation errors are calculated based on  
 564 GEOSCCM-saved total solar heating and infrared cooling rates together with the offline  
 565 radiation algorithm:

$$566 \quad \Delta \mathbf{T}^{err1} = \mathbf{Z} \cdot \Delta \mathbf{S}^{err} \quad \text{and} \quad \Delta \mathbf{T}^{err2} = \mathbf{Z} \cdot (-\Delta \mathbf{R}^{err}), \quad (20a,b)$$

568 where  $\Delta \mathbf{S}^{err}$  and  $\Delta \mathbf{R}^{err}$  are respectively the changes in total radiative heating and cooling rates  
 569 between two states 1 and 2 derived from the offline and GEOSCCM online radiation algorithms

$$570 \quad \Delta \mathbf{S}^{err} = \Delta \mathbf{S}^{off} - \Delta \mathbf{S}^{ccm} \quad \text{and} \quad \Delta \mathbf{R}^{err} = \Delta \mathbf{R}^{off} - \Delta \mathbf{R}^{ccm}. \quad (21a,b)$$

572 It has been suggested that the error terms are mostly contributed from the different averaging  
 573 procedures between the online and offline calculations (Taylor *et al.* 2013; Sejas *et al.* 2014).  
 574 Additional errors will also contribute to partial temperature changes due to radiation errors when  
 575 different radiation algorithms are adopted for the online and offline radiative heating and cooling  
 576 rate calculations. The error introduced by inferring  $\Delta \mathbf{Q}$  from radiative forcing evaluated from  
 577 the offline radiative transfer model calculations can be estimated and analyzed by a comparison  
 578 with that derived directly from CCM outputs saved during runtime (Sejas *et al.* 2014).

579 In this paper, we choose the same output time periods of 2002-2003 (near solar  
 580 maximum) and 2008-2009 (solar minimum) from one GEOSCCM simulation as those for



581 SABER measurements used in the last section to perform the MCFRAM analysis. In Fig. 8, we  
 582 show the variation in effective albedo of the surface and lower atmosphere scaled by the  
 583 diurnally averaged solar radiation  $(S_0\bar{\mu})\Delta\omega_0$  as a function of month and latitude over the 24-  
 584 month period. The figure shows a typical variation of  $\sim 5 \text{ W m}^{-2}$  that is about 1% of the globally  
 585 averaged solar flux  $(S_0/4)$  and is one order of magnitude greater than the variation in solar  
 586 constant for the 11-year solar cycle (Lean 1991). The figure shows significant geographic and  
 587 transient variations with peak values appearing near equatorial and summer polar areas where the  
 588 maximum mean solar fluxes are deposited. Climate change or the system's feedback response is  
 589 often associated with a radiative forcing scaled by the changes in the total radiation flux. Since  
 590 the energy deposition in the atmosphere at different wavelengths varies drastically with spatial  
 591 and temporal distributions of absorbers, the change in the input solar energy may not be able to  
 592 fully represent how the system responds. On the other hand, the MCFRAM analysis based on  
 593 Eqs. (10)-(11) together with Table 1 provides us with a complete view of the system response in  
 594 the same variable and units under an observational constraint of the measured total temperature  
 595 change  $(\Delta\mathbf{T}^{total})$ .

596 In Fig. 9, we show all the partial temperature change components in Table 1 in the middle  
 597 atmosphere below 70 km that can be directly calculated based on GEOSCCM output fields and  
 598 the offline JHU/APL radiation algorithm. Panels (a)-(j) correspond to the first 10 rows in Table 1  
 599 plus Eqs. (20a, b) but excluding  $\Delta\mathbf{T}^{O_2}$ , which is negligible below the mesopause. Panels (k) and  
 600 (l) are respectively the partial temperature changes due to all radiative processes  $(\Delta\mathbf{T}^{rad})$  with the  
 601 offline radiation algorithm only  $(\Delta\mathbf{T}_{offline}^{rad})$  and that including the online correction terms  
 602  $(\Delta\mathbf{T}_{online}^{rad})$ , *i.e.*

$$603 \quad \Delta\mathbf{T}_{online}^{rad} = \Delta\mathbf{T}_{offline}^{rad} - \Delta\mathbf{T}^{err1} - \Delta\mathbf{T}^{err2}. \quad (22)$$

605 Panel (m) sums all the  $\Delta\mathbf{T}^{(n)}$  components that can be directly calculated

$$606 \quad \Delta\mathbf{T}_{online}^{sum} = \Delta\mathbf{T}_{online}^{rad} + \Delta\mathbf{T}^{w*} + \Delta\mathbf{T}^{\ominus}. \quad (23)$$

608 Panels (n) and (o) are the residual partial temperature changes corresponding to the online  
609 versions of  $\Delta T^{eddy}$  and  $\Delta T^{non-rad}$  defined in Table 1, respectively.

610 We first note that the overall patterns and magnitudes of the partial temperature changes  
611  $\Delta T^{CO_2}$  and  $\Delta T^{F107}$  (Figs. 9a and 9c) that are primarily induced by the variations of the external  
612 forcing are nearly identical to those derived by SABER measurements in the common domain  
613 (Figs. 6a and 6c). However, GEOSCCM shows an additional strengthening in partial temperature  
614 change associated with the CO<sub>2</sub> cooling in the available high latitude and polar regions,  
615 especially in the southern hemisphere mesosphere where the coldest temperature often occurs  
616 near the summer mesopause (Lubken 1999; Lubken *et al.* 1999). This is caused by a non-  
617 localized heat exchange between the warmer stratopause and colder mesopause when the CO<sub>2</sub> 15  
618  $\mu\text{m}$  band transmission behaves transparently and the summer mesopause receives net radiative  
619 heating from the stratopause (Zhu *et al.* 1992). An increase in CO<sub>2</sub> concentration increases the  
620 atmospheric opacity that leads to a reduction in summer mesopause net heating rate.  
621 Furthermore, there exists a local maximum in CO<sub>2</sub> 15  $\mu\text{m}$  cooling rate near the winter polar  
622 mesopause due to the combination of local thermodynamic equilibrium conditions, a near  
623 uniform temperature, and a near transparent emission to space (Zhu 1994). This too contributes  
624 to the strengthening in  $\Delta T^{CO_2}$  in the high-latitude and polar mesosphere regions. There exists a  
625 significant difference in  $\Delta T^{O_3}$  between GEOSCCM fields (Fig. 9b) and SABER measurements  
626 (Fig. 6b). This is not surprising because the middle atmosphere O<sub>3</sub> and its variability are very  
627 sensitive to a strong nonlinear coupling between photochemistry and dynamics. For example, the  
628 largely off-set peaks in  $\Delta T^{O_3}$  in the equatorial lower stratosphere may well reflect the degree of  
629 fidelity of GEOSCCM simulation to the equatorial quasi-biennial oscillation phenomenon.

630 The partial temperature change  $\Delta T^{H_2O}$  as shown in Fig. 9d makes a much smaller  
631 contribution and is negative in the low latitude but positive in part of the midlatitude in the  
632 middle atmosphere. Middle atmosphere H<sub>2</sub>O may increase with time as a result of increasing  
633 CH<sub>4</sub> in the troposphere (Zhu *et al.* 1999). Its decadal change could also be well correlated to the

634 equatorial sea surface temperature that largely determines the coldness of tropopause to limit the  
 635 direct entry of H<sub>2</sub>O into the stratosphere (Solomon *et al.* 2010). The existence of large regions of  
 636 both positive and negative  $\Delta T^{H_2O}$  in the middle atmosphere is an indication that both processes  
 637 play important roles in determining H<sub>2</sub>O concentration in the time period of 2002-2009. The  
 638 contribution by the lower atmosphere effective albedo  $\Delta T^{\omega_0}$  is even smaller than  $\Delta T^{H_2O}$  by  
 639 nearly one order of magnitude and changes are largely confined in the stratosphere (Fig. 9e).  
 640 Comparison between Fig. 8 and Figs. 9a-e gives us one example that the MCFRAM with its key  
 641 additive property provides us with a more direct and quantitative insight into the relative  
 642 importance of different factors of climate forcing and feedback processes when they are  
 643 constrained under the same scale with the same units. Panels (f) and (g) represent the part of the  
 644 dynamical effects on the atmospheric thermal response that can be easily evaluated based on the  
 645 available model output fields. As we have already conjectured in discussing the MCFRAM  
 646 applications to the SABER measurements, the directly calculable components of  $\Delta T^{non-rad}$  are  
 647 overwhelmingly large with the majority of the contributions coming from  $\Delta T^{w*}$ . We note that  
 648 the peak values of  $\Delta T^{w*}$  occur near polar areas and arctic and antarctic circles, where the  
 649 spherical geometry may lead to unusually large variability in solar heating rate or flow  
 650 divergence, both in the real atmosphere and in numerical models.

651 Panels (h) and (i) in Fig. 9 show the partial temperature changes,  $\Delta T^{err1}$  and  $\Delta T^{err2}$ , due  
 652 to differences in heating and cooling rates between the offline and online calculations,  
 653 respectively. The figures show that the differences are small in most regions of the middle  
 654 atmosphere except  $\Delta T^{err1}$  near the low latitude upper boundary and  $\Delta T^{err2}$  near the polar area.  
 655 We note that the heating rate difference associated with  $\Delta T^{err1}$  by the solar radiation near  
 656 model's upper boundary is sensitive to the shielding effect of the solar flux by the absorber  
 657 column above the upper boundary. Furthermore, the sensitivity decreases with increasing latitude  
 658 as the slant path also increases. The high latitude cooling rate difference associated with  $\Delta T^{err2}$   
 659 is likely sensitive to the non-localized heat exchange when the vertical temperature gradient is

660 large. Specifically, the heat exchange by the CO<sub>2</sub> 15-μm band becomes transparent above the  
 661 stratopause for a uniform CO<sub>2</sub> mixing ratio distribution whereas the O<sub>3</sub> 9.6 μm band emission  
 662 could be transparent in the entire atmosphere in regions where the O<sub>3</sub> concentration is low (Zhu  
 663 *et al.* 1991, 1992, Zhu 1994). The issue of  $\Delta\mathbf{T}^{err1}$  and  $\Delta\mathbf{T}^{err2}$  will be further pursued in the next  
 664 stage of investigation.

665 Figure 9j shows the measurable temperature difference ( $\Delta\mathbf{T}^{total}$ ) between the two  
 666 equilibrium states 1 and 2, which is the difference of the model output temperature fields.  
 667 Comparing with Fig. 5c, we note that both the modeled and SABER measured  $\Delta\mathbf{T}^{total}$  show  
 668 positive-negative paired peaks of the same magnitudes near 50° latitudes and equatorial lower  
 669 stratosphere. We note that  $\Delta\mathbf{T}^{total}$  provides an observational constraint and a unified or a  
 670 standard scale to all the other sensitivity responses in the MCFRAM analysis. Recall that  
 671 MCFRAM (or CFRAM) was developed from the energy budget equation (1) or (2). In addition  
 672 to changes in the energy budget due to all the parameter variations shown in panels (a)-(g), the  
 673 most prominent and well behaved one is the change in cooling rate and the diffusive heat  
 674 exchange caused by the variation of atmospheric temperature  $\mathbf{T}$ . The well-behaved nature of  
 675  $\Delta(\mathbf{R}-\mathbf{Q}_{mol})$  with respect to  $\mathbf{T}$  in Eq. (4) makes the generalized damping matrix  $\mathbf{A}$  always  
 676 invertible. Furthermore, the temperature  $\mathbf{T}$  is a directly measurable and most common variable.  
 677 These two features can be considered the underpinning for MCFRAM that exclusively separates  
 678 the temperature component of variation in the energy budget from all the other components in  
 679 Eq. (4) and set it to be a standard scale to be compared to all the other feedback responses.  
 680 Panels (k) and (l) in Fig. 9 show the partial temperature changes due to radiative processes based  
 681 on offline and online radiation algorithms,  $\Delta\mathbf{T}_{offline}^{rad}$  and  $\Delta\mathbf{T}_{online}^{rad}$  ( $=\Delta\mathbf{T}_{offline}^{rad}-\Delta\mathbf{T}^{err1}-\Delta\mathbf{T}^{err2}$ ),  
 682 respectively. We note that the magnitude of  $\Delta\mathbf{T}^{rad}$  increases with altitude, which is consistent  
 683 with that of the measurable  $\Delta\mathbf{T}^{total}$ . However, there exist significant differences in spatial  
 684 structure contributed from the partial temperature changes due to non-radiative processes  
 685  $\Delta\mathbf{T}^{non-rad}$ . Since  $\Delta\mathbf{T}^{non-rad}$  is dependent on atmospheric motion that is strongly nonlinear and

686 contains many different scales, we expect the magnitude  $\Delta\mathbf{T}^{non-rad}$  to be reduced when an  
 687 ensemble average is taken for the MCFRAM analysis to the output fields from many different  
 688 runs of GEOSCCM in our future investigations.

689 Among all the components  $\Delta\mathbf{T}^{(n)}$  listed in Table 1 the biggest component that can be  
 690 directly calculated as shown in Fig. 9f is  $\Delta\mathbf{T}^{w*}$ . Its typical localized value is nearly an order of  
 691 magnitude greater than temperature changes  $\Delta\mathbf{T}^{total}$  or  $\Delta\mathbf{T}^{rad}$  as shown in Fig. 9j-9l. As a result,  
 692 if we sum up all the terms in Table 1 that can be directly calculated,  $\Delta\mathbf{T}^{(1-8)}$  as shown in Fig. 9m  
 693 in its online version, then its overall spatial distribution will be dominated by that of  $\Delta\mathbf{T}^{w*}$ . The  
 694 last two panels (n) and (o) in Fig. 9 correspond to two last partial temperature changes in Table  
 695 1,  $\Delta\mathbf{T}^{eddy}$  and  $\Delta\mathbf{T}^{non-rad}$ , calculated by the residual method.  $\Delta\mathbf{T}^{eddy}$  is due to dynamical heating  
 696 contributed by the unresolved eddies and horizontal winds.  $\Delta\mathbf{T}^{non-rad}$  is  $\Delta\mathbf{T}^{eddy}$  plus the partial  
 697 temperature changes associated with the adiabatic cooling due to vertical motion that can be  
 698 calculated based on the column profiles. We see again that  $\Delta\mathbf{T}^{eddy}$  largely cancels  $\Delta\mathbf{T}^{w*}$   
 699 contained in  $\Delta\mathbf{T}^{(1-8)}$  mostly due to the energy perturbation associated with the horizontal  
 700 motions. Since the localized partial temperature changes due to radiative processes  $\Delta\mathbf{T}^{rad}$  shown  
 701 in panel (l) is smaller than the local values of  $\Delta\mathbf{T}^{total}$  shown in panel (j), the overall magnitude  
 702 and spatial structure of  $\Delta\mathbf{T}^{non-rad}$  as shown in the last panel (o) is similar to those of  $\Delta\mathbf{T}^{total}$ ,  
 703 indicating dynamical processes dominate the local structure of the total partial temperature  
 704 change. This is also consistent with our previous analysis to SABER measurements where Fig.  
 705 5c and Fig. 6d show large similarities in their overall magnitude and spatial structure.

706 In Fig. 10, we show the globally averaged partial temperature changes presented in Fig.  
 707 9. Several major features are consistent with those derived from the SABER measurements as  
 708 shown in Fig. 7: (i)  $\Delta\mathbf{T}^{F107}$  makes the largest contribution above  $\sim 40$  km, (ii)  $\Delta\mathbf{T}^{CO_2}$  is negative  
 709 at all altitudes whereas  $\Delta\mathbf{T}^{O_3}$  is positive in some part of the altitude range, (iii) the globally  
 710 averaged  $\Delta\mathbf{T}^{w*}$  due to atmospheric circulation makes a small contribution to the global mean  
 711 climate change in the middle atmosphere below 70 km, which is primarily driven by radiative

712 processes. In addition to  $\Delta\mathbf{T}^{w*}$ , the three more terms  $\Delta\mathbf{T}^{\text{H}_2\text{O}}$ ,  $\Delta\mathbf{T}^\ominus$  and  $\Delta\mathbf{T}^{\omega_0}$  have been directly  
713 calculated based on the GEOSCCM output fields. Since the globally averaged values of these  
714 terms are all smaller than  $\Delta\mathbf{T}^{rad}$ , our major results derived from the SABER measured  $\mathbf{T}$  and  $\text{O}_3$   
715 fields remain valid. We have already mentioned that it is generally unavoidable to adopt an  
716 offline radiation algorithm to perform the MCFRAM analysis. We note that  $\Delta\mathbf{T}^{err2}$  due to  
717 cooling rate difference is negligibly small, and  $\Delta\mathbf{T}^{err1}$  increases rapidly near the model's upper  
718 boundary, which in turn leads to a large deviation of  $\Delta\mathbf{T}^{rad}$  from  $\Delta\mathbf{T}^{total}$  near the upper  
719 boundary. We note that all the model fields in GEOSCCM, including the atmospheric  
720 temperature, have been integrated subject to the influence of a set of prescribed boundary  
721 conditions. On the other hand, the magnitude of  $\Delta\mathbf{T}^{rad}$  derived from the SABER measurements  
722 as shown in Fig. 7 does not systematically increase with the altitude below 80 km, indicating the  
723 effect of boundary condition on the heating rate calculations for GEOSCCM fields. We will  
724 pursue this issue in our follow-up investigations.

## 725 **5. Summary**

726 In this study, we have extended the Climate Feedback-Response Analysis Method  
727 (CFRAM) for the coupled atmosphere-surface system to the middle atmosphere. The Middle  
728 atmosphere CFRAM (MCFRAM) is built upon the atmospheric energy equation per unit mass  
729 with radiative heating and cooling rates as its major thermal energy sources. In addition,  
730 molecular thermal conduction is added to the energy equation when the upper boundary is  
731 extended beyond the mesopause. MCFRAM preserves the unique feature of an additive property  
732 for the original CFRAM in which the sum of all partial temperature changes equals the observed  
733 temperature change. By introducing the generalized damping ( $\mathbf{A}$ ) and relaxation ( $\mathbf{Z}$ ) matrices to  
734 the basic MCFRAM equation, the relationship between the fundamental quantity of the partial  
735 temperature change ( $\Delta\mathbf{T}^{(n)}$ ) and its physical cause of energy perturbation ( $\Delta\mathbf{F}^{(n)}$ ) is  
736 quantitatively clarified by the well-documented theory of radiative damping of thermal  
737 disturbance in the middle atmosphere. Specifically, we show that  $\mathbf{A}$  serves as a filter that

738 smoothes the small-scale structure in  $\Delta\mathbf{F}^{(n)}$ . In addition, it is shown that for a given energy  
739 perturbation the maximum response in temperature change occurs when the energy perturbation  
740 is located at the place where the cooling rate of the mean state reaches its minimum value.

741 The newly developed MCFRAM is applied to two sets of two-dimensional data. One is  
742 the zonal mean  $T$  and  $O_3$  fields in the middle atmosphere derived from SABER measurements in  
743 the low and midlatitudes averaged over yaw cycles. The other is the zonal mean fields saved  
744 from GEOSCCM simulations. It is found that the spatial structure of the temperature responses  
745 to variations of  $CO_2$ ,  $O_3$  and solar flux are different.  $\Delta\mathbf{T}^{CO_2}$  closely follows temperature  
746 distribution in most of the middle atmosphere because the cool-to-space approximation is valid  
747 for an atmosphere with uniformly distributed  $CO_2$  mixing ratio. Both the solar radiation heating  
748 and 9.6- $\mu\text{m}$  band cooling by  $O_3$  affect  $\Delta\mathbf{T}^{O_3}$  in about the same order of magnitude, both  
749 processes strongly influenced by  $O_3$  distribution.  $\Delta\mathbf{T}^{F107}$  monotonically increases with altitude  
750 due to the fact that the solar UV fluxes of greater variations at shorter wavelengths are generally  
751 absorbed at higher altitudes. The two periods used to derive the statistical equilibrium states are  
752 2002-2003 and 2008-2009, corresponding to near solar maximum and solar minimum,  
753 respectively. The  $CO_2$  mixing ratio between these two periods increases from  $\sim 374.7$  ppmv to  
754  $\sim 386.3$  ppmv. It is consistently found by both datasets that for a half cycle span of the 11-year  
755 solar cycle the largest component of the partial temperature changes ( $\Delta\mathbf{T}^{(n)}$ ) in the middle  
756 atmosphere is the one due to the variation of the input solar flux ( $\Delta\mathbf{T}^{F107}$ ). The effect of  
757 increasing  $CO_2$  always cools the middle atmosphere with time ( $\Delta\mathbf{T}^{CO_2} < 0$ ). On the other hand,  
758 depending on the relative importance of  $O_3$  heating and cooling rates,  $\Delta\mathbf{T}^{O_3}$  could be either  
759 positive or negative. The MCFRAM analysis to GEOSCCM fields suggests that  $\Delta\mathbf{T}^{H_2O}$  makes a  
760 minor contribution to the total temperature change observed from the atmosphere ( $\Delta\mathbf{T}^{total}$ ). The  
761 partial temperature change due to the variation of the effective albedo of the surface and lower  
762 atmosphere to the solar radiation ( $\Delta\mathbf{T}^{\omega_0}$ ) is negligibly small in comparison with those by other  
763 factors.

764           Because of the lack of all the required parameters in the input datasets, the partial  
765 temperature change due to non-radiative processes ( $\Delta T^{non-rad}$ ) often needs to be evaluated by  
766 either an energy or a temperature residual approach. Such an approach is well-founded due to the  
767 existence of the additive property for the generic energy equation (3) or the basic MCFRAM  
768 equation (10) to temperature changes.  $\Delta T^{non-rad}$  for the SABER measurements includes all  
769 dynamical effects whereas three individual components in  $\Delta T^{non-rad}$  can be evaluated separately  
770 based on the GEOSCCM model outputs. In both cases, the typical magnitude of  $\Delta T^{non-rad}$  is  
771 significantly greater than any component consisting of partial temperature changes due to  
772 radiation processes ( $\Delta T^{rad}$ ). However, the global average of  $\Delta T^{non-rad}$  is much smaller than that  
773 of  $\Delta T^{rad}$  below  $\sim 70$  km, indicating the lack of vertical transport of energy by eddies or by global  
774 mean vertical velocity. Physically, this means that the globally averaged climate change in the  
775 middle atmosphere below  $\sim 70$  km is thermally driven. This also means that the globally  
776 averaged partial temperature change due to all radiative processes is approximately equal to the  
777 observed temperature change. It ranges from  $-0.5$  K near 25 km to  $-1.0$  K near 70 km from the  
778 near solar maximum to the solar minimum.

779

## 780 **ACKNOWLEDGMENTS**

781           This research was supported by NASA Living With a Star Program under Grant  
782 NNX13AF91G and NASA Geospace Science Program under Grant NNX13AE33G to The Johns  
783 Hopkins University Applied Physics Laboratory. Constructive comments from Jae N. Lee on the  
784 original manuscript are greatly appreciated.

785



786 **REFERENCES:**

- 787 Aquila, V., L. D. Oman, R. S. Stolarski, P. R. Colarco, and P. A. Newman, 2012: Dispersion of  
788 the volcanic sulfate cloud from a Mount Pinatubo–like eruption. *J. Geophys. Res.*, **117**,  
789 D06216. doi:10.1029/2011JD016968.
- 790 Aquila, V., L. D. Oman, R. S. Stolarski, A. R. Douglass, and P. A. Newman, 2013: The response  
791 of ozone and nitrogen dioxide to the eruption of Mt. Pinatubo at southern and northern  
792 midlatitudes. *J. Atmos. Sci.*, **70**, 894–900. doi:10.1175/JAS-D-12-0143.1.
- 793 Banks, P. M. and G. Kockarts, 1973: *Aeronomy, Part B*. Academic Press, New York, 355 pp.
- 794 Butchart, N., *et al.*, 2006: Simulations of anthropogenic change in the strength of the Brewer-  
795 Dobson circulation. *Climate Dyn.*, **27**, 727-741.
- 796 Cai, M., and J. Lu, 2009: A new framework for isolating individual feedback processes in  
797 coupled general circulation climate models. Part II: Method demonstrations and  
798 comparisons. *Climate Dyn.*, **32**, 887-900, doi: 10.1007/s00382-008-0424-4.
- 799 Cogley, A. C., and W. J. Borucki, 1976: Exponential approximation for daily average solar  
800 heating or photolysis. *J. Atmos. Sci.*, **33**, 1347-1356.
- 801 Douglass, A. R., C. J. Weaver, R. B. Rood, and L. Coy, 1996: A three-dimensional simulation of  
802 the ozone annual cycle using winds from a data assimilation system, *J. Geophys. Res.*, **101**,  
803 1463-1474.
- 804 Fels, S. B., 1982: A parameterization of scale-dependent radiative damping rates in the middle  
805 atmosphere. *J. Atmos. Sci.*, **39**, 1141-1152.
- 806 Fels, S. B., 1987: Response of the middle atmosphere to changing O<sub>3</sub> and CO<sub>2</sub> – A speculative  
807 tutorial. In *Transport Processes in the Middle Atmosphere*, G. Visconti and R. Garcia  
808 (Eds.), pp. 371-386, D. Reidel, Boston, MA.
- 809 Garcia, R. R., and W. J. Randel, 2008: Acceleration of the Brewer-Dobson circulation due to  
810 increases in greenhouse gases. *J. Atmos. Sci.*, **65**, 2731-2739.

811 Goody, R. M., and Y. L. Yung, 1989: *Atmospheric Radiation: Theoretical Basis. Second Edition.*  
812 Oxford Univ. Press, New York and Oxford, 519 pp.

813 Holton, J. R., 2004: *An Introduction to Dynamic Meteorology, Fourth Edition*, Elsevier  
814 Academic Press, New York, 535 pp.

815 Kiehl, J. T., and S. Solomon, 1986: On the radiative balance of the stratosphere. *J. Atmos. Sci.*,  
816 **43**, 1525-1534.

817 Kutepov, A. A., A. G. Feofilov, B. T. Marshall, L. L. Gordley, W. D. Pesnell, R. A. Goldberg,  
818 and J. M. Russell III, 2006: SABER temperature observations in the summer polar  
819 mesosphere and lower thermosphere: Importance of accounting for the CO<sub>2</sub> v<sub>2</sub> quanta V-V  
820 exchange, *Geophys. Res. Lett.*, **33**, L21809, doi:10.1029/2006GL026591.

821 Lean, J., 1991: Variations in the Sun's radiative output. *Rev. Geophys.*, **29**, 505-535.

822 Liou, K. N., 2002: *An Introduction to Atmospheric Radiation*. 2nd Edition. Academic Press, New  
823 York, 583 pp.

824 Lu, J., and M. Cai, 2009: A new framework for isolating individual feedback processes in  
825 coupled general circulation climate models. Part I: Formulation. *Climate Dyn.*, **32**, 873-  
826 885, doi: 10.1007/s00382-008-0425-3.

827 Lu, J. and M. Cai, 2010: Quantifying contributions to polar warming amplification in an  
828 idealized coupled general circulation model. *Clim. Dyn.*, **34**, 449-687.

829 Lubken, F. -J, 1999: Thermal structure of the Arctic summer mesosphere. *J. Geophys. Res.*, **104**  
830 (D8), 9135-9149.

831 Lubken, F. -J, M. J. Jarvis, G. O. L. Jones, 1999: First in situ temperature measurements at the  
832 Antarctic summer mesopause. *Geophys. Res. Lett.*, **26**, 3581-3584.

833 Meier, R. R., D. E. Anderson, M. Nicolet, 1982: Radiation field in the troposphere and  
834 stratosphere from 240 to 1000 nm. I. General analysis. *Planet. Space Sci.*, **30**, 923-933.

835 Molod, A., L. Takacs, M. Suarez, J. Bacmeister, I.-S. Song, and A. Eichmann, 2012: The GEOS-  
836 5 Atmospheric General Circulation Model: Mean climate and development from MERRA  
837 to Fortuna, Technical Report Series on Global Modeling and Data Assimilation, 28,  
838 NASA, Greenbelt, Md.

839 Nicolet, M., R. R. Meier, and D. E. Anderson, 1982: Radiation field in the troposphere and  
840 stratosphere from 240 to 1000 nm. II. Numerical analysis. *Planet. Space Sci.*, **30**, 935-983.

841 Olaguer, E. P., H. Yang, and K. K. Tung, 1992: A reexamination of the radiative balance of the  
842 stratosphere. *J. Atmos. Sci.*, **49**, 1242-1263.

843 Pawson, S., *et al.*, 2008: Goddard Earth Observing System Chemistry-Climate Model  
844 simulations of stratospheric ozone-temperature coupling between 1950 and 2005, *J.*  
845 *Geophys. Res.*, **113**, D12103, doi:10.1029/2007JD009511.

846 Rees, M. H., 1989: *Physics and Chemistry of the Upper Atmosphere*. Cambridge Univ. Press,  
847 289 pp.

848 Rienecker, M.M., M.J. Suarez, R. Todling, J. Bacmeister, L. Takacs, H.-C. Liu, W. Gu, M.  
849 Sienkiewicz, R.D. Koster, R. Gelaro, I. Stajner, and J.E. Nielsen, The GEOS-5 data  
850 assimilation system - documentation of versions 5.0.1, 5.1.0, and 5.2.0. NASA Technical  
851 Report Series on Global Modeling and Data Assimilation, M. J. Suarez ed., NASA/TM-  
852 2008-104606, Vol. **27**, 101 pp, 2008: downloadable at [http://gmao.gsfc.nasa.gov/systems/  
853 geos5/index\\_arch.php](http://gmao.gsfc.nasa.gov/systems/geos5/index_arch.php).

854 Russell III, J. M., M. G. Mlynczak, L. L. Gordley, J. Tansock, and R. Esplin, 1999: An overview  
855 of the SAVER experiment and preliminary calibration results, *Proc. SPIE*, **3756**,  
856 doi:10.1117/12.366382, 277-288.

857 Sejas, S., M. Cai, A. Hu, G. A. Meehl, W. Washington, and P. Taylor, 2014: Individual feedback  
858 contributions to the seasonality of surface warming. *J. Climate*, doi:10.1175/JCLI-D-13-  
859 00658.1, in press.

860 Shepherd, T. G., and C. McLandress, 2011: A robust mechanism for strengthening of the  
861 Brewer-Dobson circulation in response to climate change: Critical-layer control of  
862 subtropical wave breaking. *J. Atmos. Sci.*, **68**, 784-797.

863 Soden, B. J., I. M. Held, R. Colman, K. M. Shell, J. T. Kiehl, and C. A. Shields, 2008:  
864 Quantifying climate feedbacks using radiative kernels. *J. Climate*, **21**, 3504-3520.

865 Solomon, S., K. Rosenlof, R. W. Portmann, J. S. Daniel, S. Davis, T. J. Sanford, and G. Plattner,  
866 2010: Contributions of stratospheric water vapor to decadal changes in the rate of global  
867 warming, *Science*, **327**, 1219-1223.

868 Song, X., G. J. Zhang, and Ming Cai, 2014: Characterizing the climate feedback pattern in the  
869 NCAR CCSM3-SOM using hourly data. *J. Climate*, **27**, 2912–2930.

870 Swartz, W. H., R. S. Stolarski, L. D. Oman, E. L. Fleming, and C. H. Jackman, 2012: Middle  
871 atmosphere response to different descriptions of the 11-yr solar cycle in spectral irradiance  
872 in a chemistry-climate model. *Atmos. Chem. Phys.*, **12**, 5937-5948.

873 Taylor, P. C., M. Cai, A. Hu, G. A. Meehl, W. Washington, and G. J. Zhang, 2013: A  
874 decomposition of feedback contributions to polar warming amplification. *J. Climate*, **26**,  
875 7023-7043.

876 Zhu, X., 1993: Radiative damping revisited: Parameterization of damping rate in the middle  
877 atmosphere. *J. Atmos. Sci.*, **50**, 3008-3021.

878 Zhu, X., 1994: An accurate and efficient radiation algorithm for middle atmosphere models. *J.*  
879 *Atmos. Sci.*, **51**, 3593-3614.

880 Zhu, X., 2004: Radiative transfer in the middle atmosphere and planetary atmospheres. In  
881 “*Observation, Theory and Modeling of Atmospheric Variability*” (X. Zhu et al., eds.), pp.  
882 359-396. World Scientific Pub. Co., Singapore.

883 Zhu, X., and D. F. Strobel, 1991: Radiative damping in the upper mesosphere. *J. Atmos. Sci.*, **48**,  
884 184-199.

885 Zhu, X., M. E. Summers, and D. F. Strobel, 1991: Analytic models for the ozone radiative  
886 absorption rate at 9.6  $\mu\text{m}$  in the mesosphere. *J. Geophys. Res.*, **96**(D10), 18,551-18,559.

887 Zhu, X., M. E. Summers, and D. F. Strobel, 1992: Calculation of CO<sub>2</sub> 15  $\mu\text{m}$  band atmospheric  
888 cooling rates by Curtis matrix interpolation of correlated-k coefficients. *J. Geophys. Res.*,  
889 **97**(D12), 12,787-12,797.

890 Zhu, X., J.-H. Yee, and E. R. Talaat, 2001: Diagnosis of dynamics and energy balance in the  
891 mesosphere and lower thermosphere. *J. Atmos. Sci.*, **58**, 2441-2454.

892 Zhu, X., J.-H. Yee, S. A. Lloyd, and D. F. Strobel, 1999: Numerical modeling of chemical-  
893 dynamical coupling in the upper stratosphere and mesosphere. *J. Geophys. Res.*, **104** (D19),  
894 23,995–24,011.

895 Zhu, X., D. F., Strobel, M. F. Flasar, 2008: Exchange of global mean angular momentum  
896 between an atmosphere and its underlying planet. *Planet. Space Sci.*, 56, 1524-1531.

897 Zhu, X., J.-H. Yee, W. H. Swartz, E. R. Talaat and L. Coy, 2010: A spectral parameterization of  
898 drag, eddy diffusion and wave heating for a three-dimensional flow induced by breaking  
899 gravity waves. *J. Atmos. Sci.*, **67**, 2520–2536.

900 Zhu, X., D. F. Strobel, and J. T. Erwin, 2014: The density and thermal structure of Pluto's  
901 atmosphere and associated escape processes and rates. *Icarus*, **228**, 301-314.  
902

903

904

905 Table 1. Partial temperature changes ( $\Delta\mathbf{T}^{(n)}$ ) and their physical meanings

$\Delta\mathbf{T}^{(n)}$	Definitions	Physical meanings of partial temperature changes
$\Delta\mathbf{T}^{\text{CO}_2}$	$\mathbf{Z} \cdot (-\Delta\mathbf{R}^{\text{CO}_2})$	$\Delta\mathbf{T}^{(1)}$ due to changes in $\text{CO}_2$
$\Delta\mathbf{T}^{\text{O}_3}$	$\mathbf{Z} \cdot (\Delta\mathbf{S}^{\text{O}_3} - \Delta\mathbf{R}^{\text{O}_3})$	$\Delta\mathbf{T}^{(2)}$ due to changes in $\text{O}_3$
$\Delta\mathbf{T}^{\text{F107}}$	$\mathbf{Z} \cdot \Delta\mathbf{S}^{\text{F107}}$	$\Delta\mathbf{T}^{(3)}$ due to change in downward solar radiation at TOA
$\Delta\mathbf{T}^{\text{H}_2\text{O}}$	$\mathbf{Z} \cdot (-\Delta\mathbf{R}^{\text{H}_2\text{O}})$	$\Delta\mathbf{T}^{(4)}$ due to changes in $\text{H}_2\text{O}$
$\Delta\mathbf{T}^{\text{O}_2}$	$\mathbf{Z} \cdot \Delta\mathbf{S}^{\text{O}_2}$	$\Delta\mathbf{T}^{(5)}$ due to changes in $\text{O}_2$
$\Delta\mathbf{T}^{\omega 0}$	$\mathbf{Z} \cdot \Delta\mathbf{S}^{\omega 0}$	$\Delta\mathbf{T}^{(6)}$ due to changes in troposphere albedo to the solar radiation
$\Delta\mathbf{T}^{w^*}$	$\mathbf{Z} \cdot (\Theta \Delta\mathbf{w}^*)$	$\Delta\mathbf{T}^{(7)}$ due to changes in the resolved vertical velocity
$\Delta\mathbf{T}^{\Theta}$	$\mathbf{Z} \cdot (\Delta\Theta) \mathbf{w}^*$	$\Delta\mathbf{T}^{(8)}$ due to changes in the static stability
$\Delta\mathbf{T}^{\text{eddy}}$	$\mathbf{Z} \cdot (\Delta \mathbf{Q}^{\text{eddy}})$	$\Delta\mathbf{T}^{(9)}$ due to changes in the un-resolved eddies
$\Delta\mathbf{T}^{\text{non-rad}}$	$\mathbf{Z} \cdot (\Delta\mathbf{R} - \Delta\mathbf{Q}_{\text{mol}} - \Delta\mathbf{S})$	$\Delta\mathbf{T}^{(7-9)}$ due to changes in circulation

906

907

908

909

910 FIGURE CAPTIONS

911  
912 Figure 1. Global mean temperature and ozone profiles in the middle atmosphere derived from  
913 TIMED/SABER measurements in the low and mid-latitudes over a 12-year period of 2002-2013.  
914 The TIMED/SABER measurements in the middle atmosphere are merged to the US Standard  
915 Atmosphere in the troposphere. The vertical resolution is about 0.7 km.

916  
917 Figure 2. Selected vertical eigenmodes of the generalized damping matrix  $A$  calculated from  $T$   
918 and  $O_3$  shown in Fig. 1 based on the JHU/APL radiation algorithm. The  $CO_2$  volume mixing  
919 ratio is set at 2005 level of 380 ppmv. The unit of the eigenvalues shown in the figure boxes is  
920  $day^{-1}$ .

921  
922 Figure 3. A quantitative relationship between the generalized damping rate and the vertical  
923 wavenumber at which the power spectral density is maximally peaked. Also shown in the figure  
924 are analytic fits of radiative damping given by (Zhu 1993) and a fit for diffusive damping  
925 proportional to the square of the vertical wavenumber.

926  
927 Figure 4. Linear temperature responses to three energy perturbations caused by changing three  
928 atmospheric parameters (i)  $CO_2$  volume mixing ratio is doubled from 380 ppmv to 760 ppmv,  
929 (ii)  $O_3$  mixing ratio is uniformly reduced by 50%, and (iii) solar flux index  $F_{10.7}$  is increased  
930 from 60 to 260 (in units of  $10^{-22} W m^{-2} Hz^{-1}$ ).

931  
932 Figure 5. Zonal mean  $T$  and  $O_3$  fields averaged over a 12-year period of 2002-2013 and their  
933 differences between two equilibrium states covering the periods of 2002-2003 and 2008-2009,  
934 respectively.

935  
936 Figure 6. Two dimensional distributions of partial temperature changes between two time  
937 periods of 2002-2003 and 2008-2009 due to variations in (a)  $CO_2$ , (b)  $O_3$ , (c)  $F_{10.7}$ , and (d)  
938 atmospheric circulation, respectively. (e) Equivalent partial change in vertical velocity due to

939 change in CO<sub>2</sub>. (f) Error in partial temperature change of non-radiative processes due to  
940 linearization approximation.

941  
942 Figure 7. Globally averaged partial temperature changes  $\Delta T^{CO_2}$  (dashed line with squares),  
943  $\Delta T^{O_3}$  (dashed line with triangles),  $\Delta T^{F107}$  (dashed line with circles) and their sum approximately  
944 representing  $\Delta T^{rad}$  (solid line with solid circles). (b) Globally averaged total temperature change  
945  $\Delta T^{total}$  (dashed line) and partial temperature changes  $\Delta T^{rad}$  (solid line with solid circles) and  
946  $\Delta T^{non-rad}$  (solid line with diamonds).

947  
948 Figure 8. Changes in effective albedo of the surface and lower atmosphere scaled by the  
949 diurnally averaged solar radiation between 2002-2003 and 2008-2009.

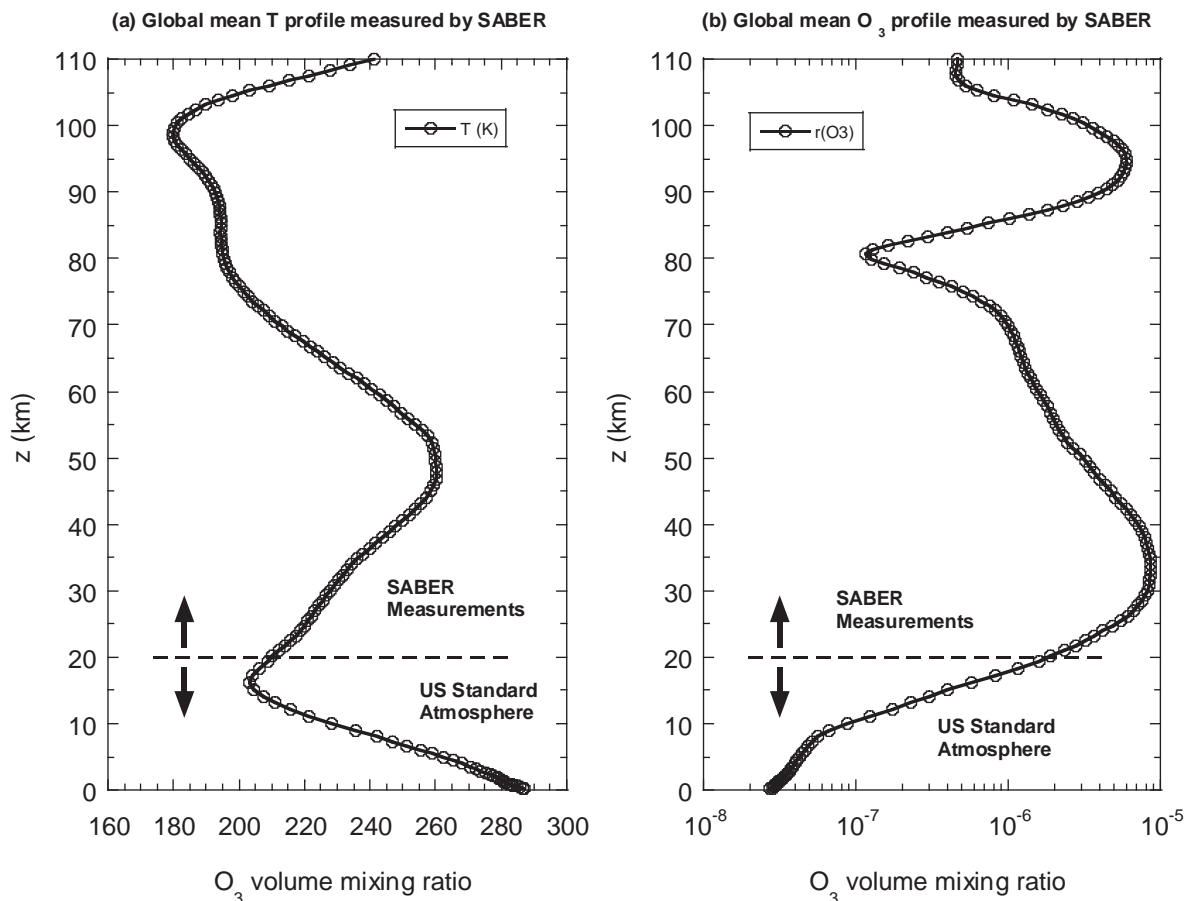
950  
951 Figure 9. Partial temperature changes caused by various energy perturbation components in the  
952 middle atmosphere. The unit in scale bars of all panels is K.

953  
954 Figure 10. Globally averaged partial temperature changes shown in Fig. 9.

955  
956



957  
958  
959

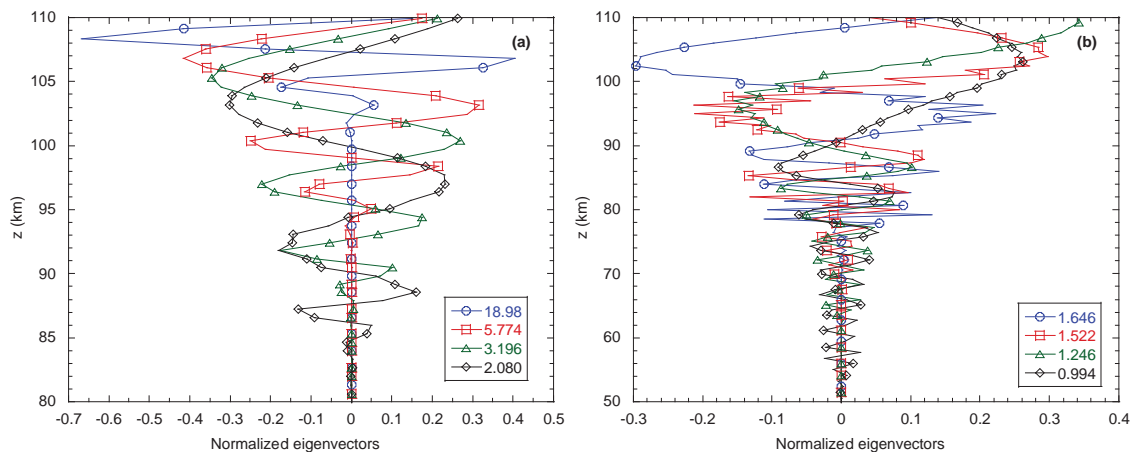


960  
961

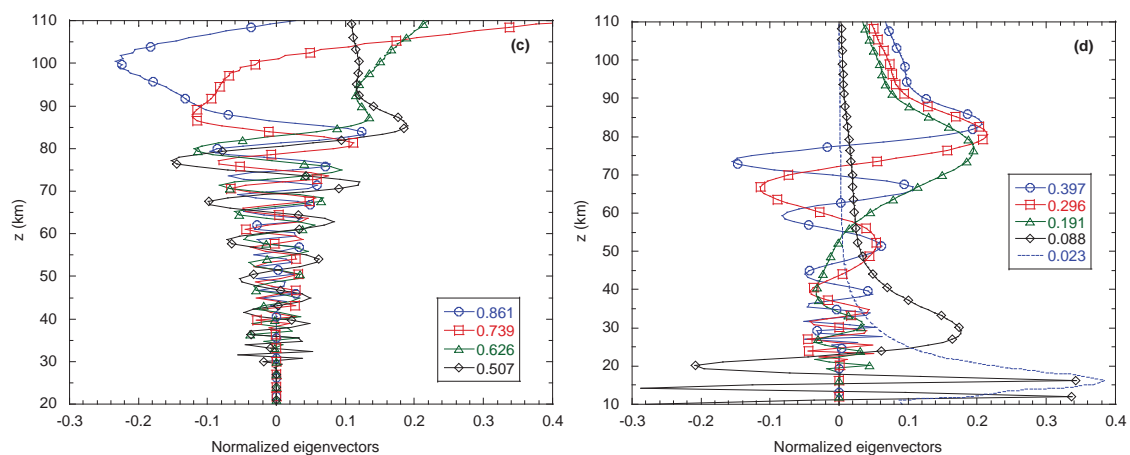
962 Figure 1. Global mean temperature and ozone profiles in the middle atmosphere  
963 derived from TIMED/SABER measurements in the low and mid-latitudes over a 12-  
964 year period of 2002-2013. The TIMED/SABER measurements in the middle  
965 atmosphere are merged to the US Standard Atmosphere in the troposphere. The vertical  
966 resolution is about 0.7 km.

967  
968  
969

970



971



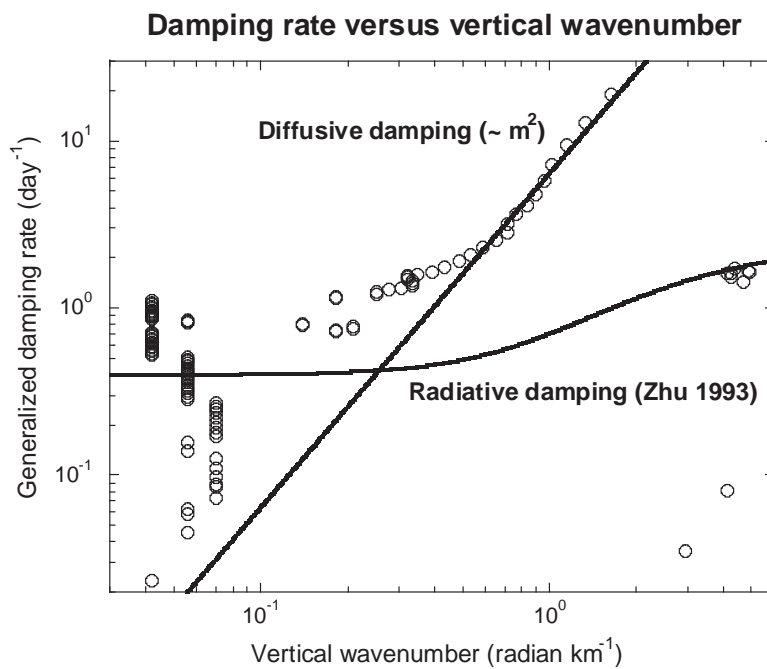
972

973

974 Figure 2. Selected vertical eigenmodes of the generalized damping matrix  $\mathbf{A}$  calculated  
975 from  $T$  and  $O_3$  shown in Fig. 1 based on the JHU/APL radiation algorithm. The  $CO_2$   
976 volume mixing ratio is set at 2005 level of 380 ppmv. The unit of the eigenvalues  
977 shown in the figure boxes is  $day^{-1}$ .

978

979



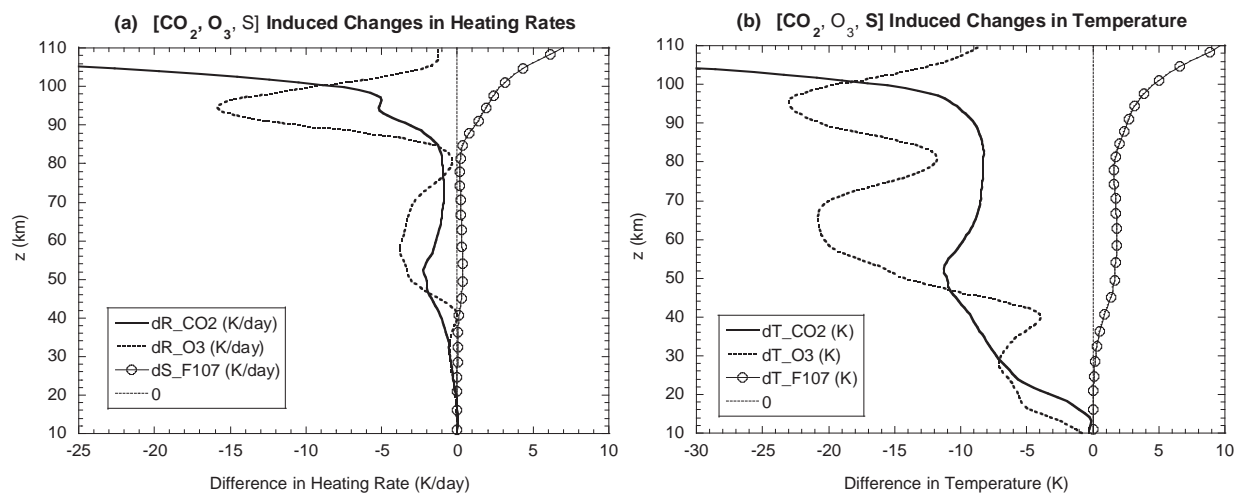
980

981

982 Figure 3. A quantitative relationship between the generalized damping rate and the  
983 vertical wavenumber at which the poser spectral density is maximally peaked. Also  
984 shown in the figure are analytic fits of radiative damping given by (Zhu 1993) and a fit  
985 for diffusive damping proportional to the square of the vertical wavenumber.

986

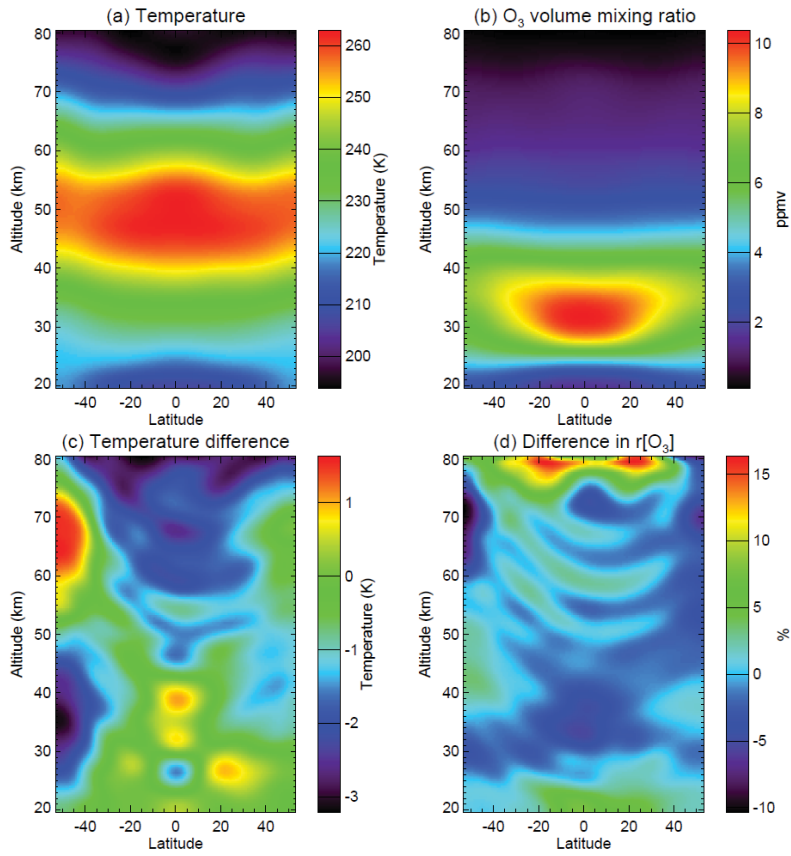
987  
988  
989



990  
991

992 Figure 4. Linear temperature responses to three energy perturbations caused by  
993 changing three atmospheric parameters (i) CO<sub>2</sub> volume mixing ratio is doubled from  
994 380 ppmv to 760 ppmv, (ii) O<sub>3</sub> mixing ratio is uniformly reduced by 50%, and (iii)  
995 solar flux index  $F_{10.7}$  is increased from 60 to 260 (in units of  $10^{-22} \text{ W m}^{-2} \text{ Hz}^{-1}$ ).

996



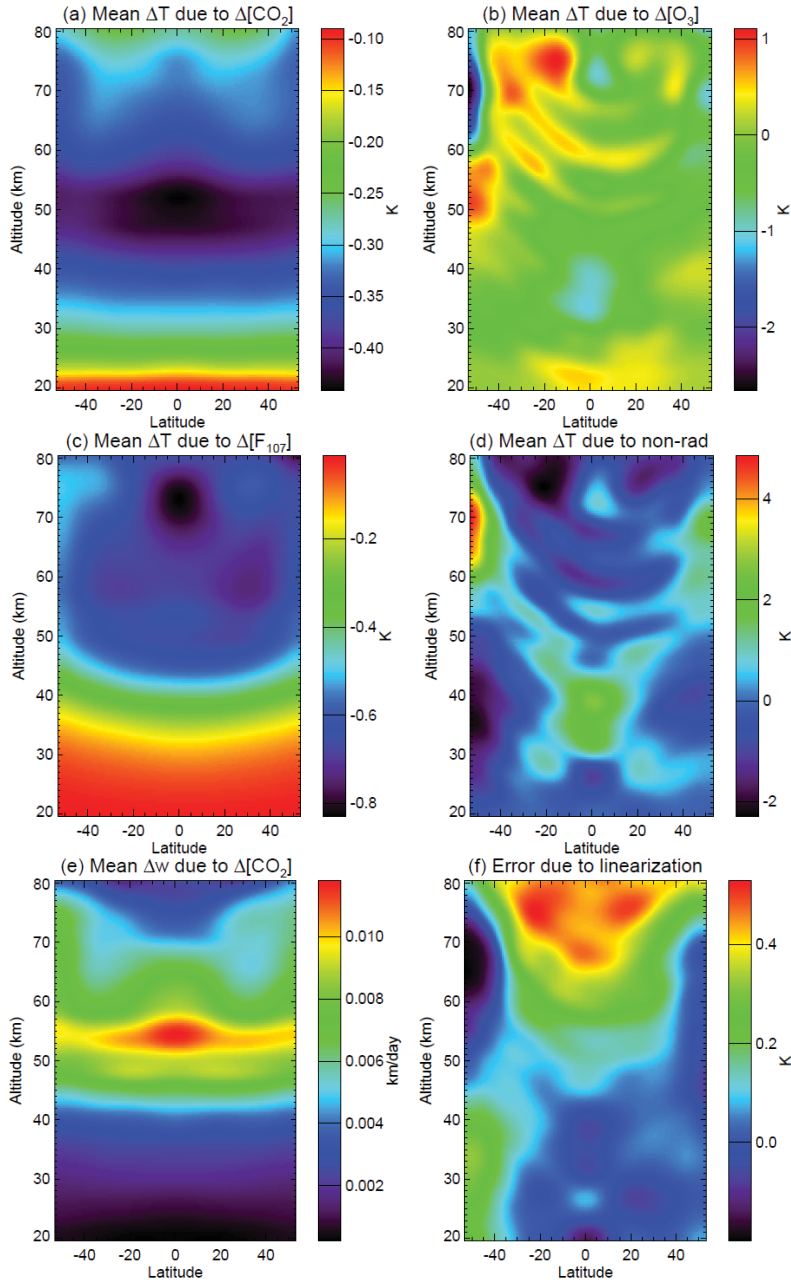
997

998  
999

1000 Figure 5. Zonal mean  $T$  and  $O_3$  fields averaged over a 12-year period of 2002-2013 and  
 1001 their differences between two equilibrium states covering the periods of 2002-2003 and  
 1002 2008-2009, respectively.

1003

1004



1005

1006

1007

1008

1009

1010

1011

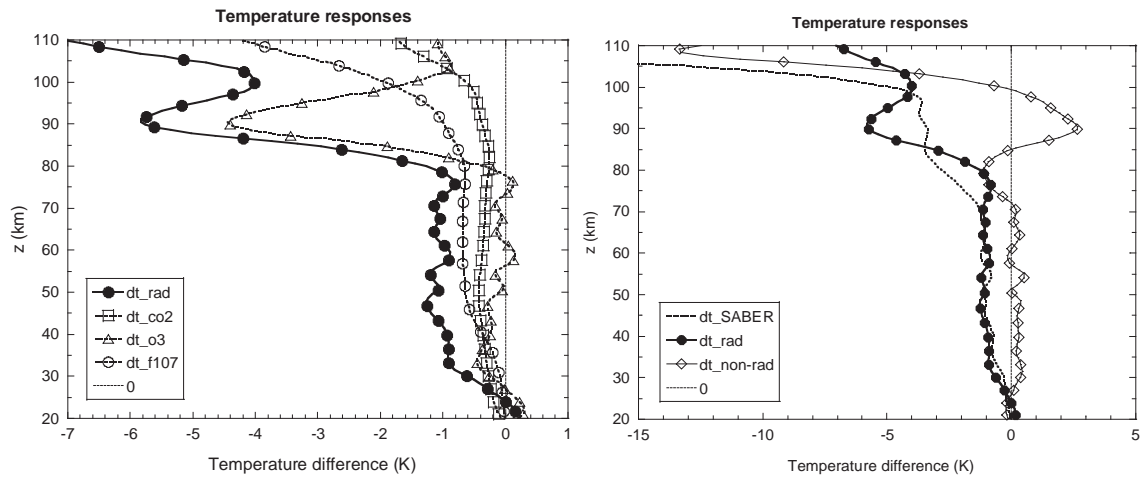
1012

1013

1014

Figure 6. Two dimensional distributions of partial temperature changes between two time periods of 2002-2003 and 2008-2009 due to variations in (a)  $\text{CO}_2$ , (b)  $\text{O}_3$ , (c)  $F_{10.7}$ , and (d) atmospheric circulation, respectively. (e) Equivalent partial change in vertical velocity due to change in  $\text{CO}_2$ . (f) Error in partial temperature change of non-radiative processes due to linearization approximation.

1015

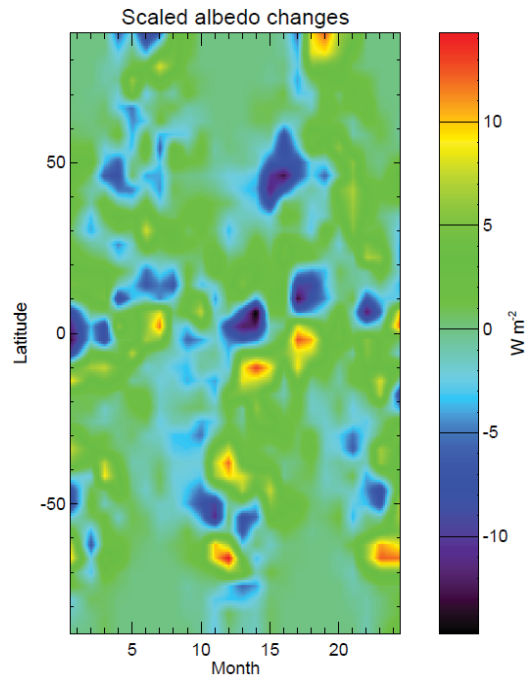


1016

1017

1018 Figure 7. (a) Globally averaged partial temperature changes  $\Delta T^{\text{CO}_2}$  (dashed line with  
1019 squares),  $\Delta T^{\text{O}_3}$  (dashed line with triangles),  $\Delta T^{\text{F}107}$  (dashed line with circles) and their  
1020 sum approximately representing  $\Delta T^{\text{rad}}$  (solid line with solid circles). (b) Globally  
1021 averaged total temperature change  $\Delta T^{\text{total}}$  (dashed line) and partial temperature changes  
1022  $\Delta T^{\text{rad}}$  (solid line with solid circles) and  $\Delta T^{\text{non-rad}}$  (solid line with diamonds).

1023

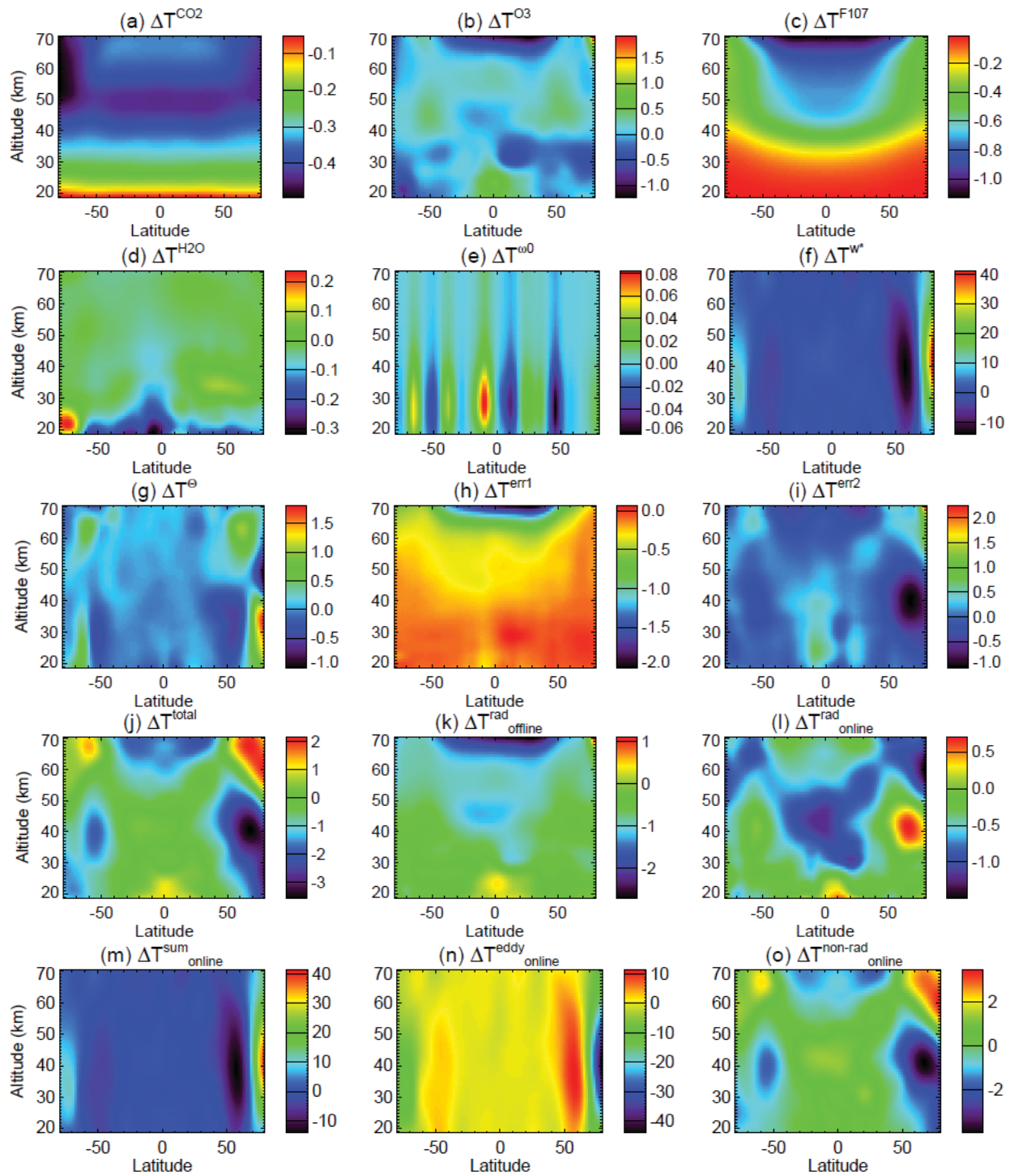


1024  
1025

1026 Figure 8. Changes in effective albedo of the surface and lower atmosphere scaled by the  
1027 diurnally averaged solar radiation between 2002-2003 and 2008-2009.

1028  
1029





1030

1031

1032

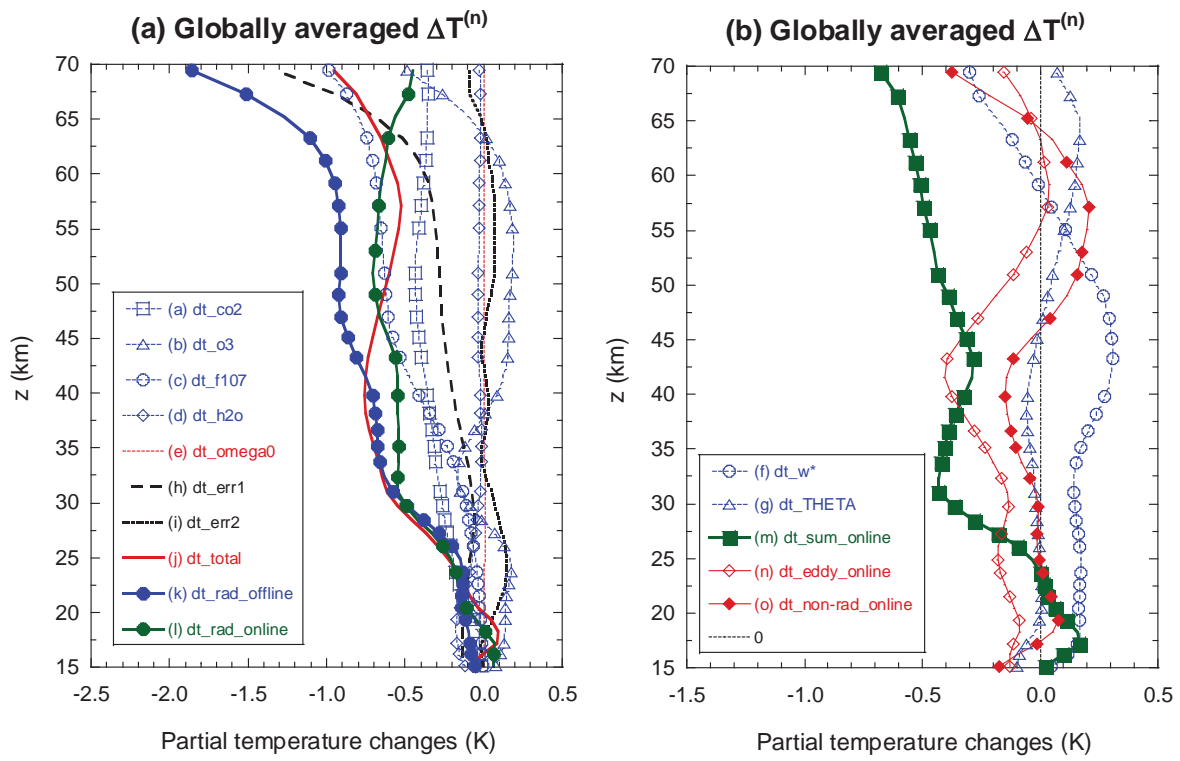
1033

1034

1035

1036 Figure 9. Partial temperature changes caused by various energy perturbation  
 1037 components in the middle atmosphere. The unit in scale bars of all panels is K.

1038



1040

1041

1042

Figure 10. Globally averaged partial temperature changes shown in Fig. 9.

1043